minerals

MDPI

Article

U-Pb Dating, Lead Isotopes, and Trace Element Composition of Pyrite Hosted in Black Shale and Magmatic Rocks, Malaysia: Implications for Orogenic Gold Mineralization and Exploration

Charles Makoundi [1,2], Khin Zaw [1] and Zakaria Endut [2,*]

[1] Centre for Ore Deposit and Earth Science, University of Tasmania, Private Bag 126, Hobart, TAS 7001, Australia
[2] School of Materials and Mineral Resources Engineering, Universiti Sains Malaysia, Nibong Tebal 14300, Penang, Malaysia
* Correspondence: zakaria.endut@usm.my

Abstract: Several orogenic/sediment-hosted gold deposits are widely distributed in the Central Belt of Peninsular Malaysia. This study combines U-Pb dating with the isotope composition of lead as well as gold content in ore and magmatic rock-hosted pyrite. It aims to investigate the age of gold mineralization and possibly establish a link between gold mineralization and magmatic intrusion in the district. The results show that the S-type magmatic rocks yield crystallisation ages ranging from 204.1 ± 4.7 Ma to 223 ± 3.2 Ma with low magnetic susceptibility measurements below 3×10^{-3} SI unit. These ages fit within the 200–250 Ma Pb-Pb model age of the Pb isotopic composition of K-feldspars. Pyrite trace element mapping has shown that gold and lead show zoning patterns occurring at the same time in pyrite. The Pb isotope composition of the cores of pyrite grains indicate that the approximate model age of gold mineralization is 200 Ma. This age is close to 197–199 Ma (Early Jurassic), previously determined by K-Ar dating of sericite which was interpreted to be the age of gold mineralization. In this study, gold content varies up to 793 ppb in the analysed magmatic rock-hosted pyrites, indicative of a likely magmatic contribution to gold mineralization.

Keywords: zircon; gold; lead; age; magma; isotope; Permian; Indosinian; Malaysia

check for updates

Citation: Makoundi, C.; Zaw, K.; Endut, Z. U-Pb Dating, Lead Isotopes, and Trace Element Composition of Pyrite Hosted in Black Shale and Magmatic Rocks, Malaysia: Implications for Orogenic Gold Mineralization and Exploration. *Minerals* **2023**, *13*, 221. https://doi.org/10.3390/min13020221

Academic Editor: Yamirka Rojas-Agramonte

Received: 6 January 2023
Revised: 28 January 2023
Accepted: 30 January 2023
Published: 2 February 2023

1. Introduction

Peninsular Malaysia comprises several gold deposits which are currently mined and extensively explored (Figure 1). The tectonic setting of the Malaysian Peninsula is characterized by three belts namely the Western, Central and Eastern Belts. The Paleozoic sedimentary formations and magmatic rocks are widely exposed across the peninsula (Figure 1). For several decades, metallogenic research has been undertaken in Malaysia to understand the ore genesis with a particular emphasis on gold [1–8].

To date, gold mining has been one of the key economic drivers in Malaysia. Hence, constraining the metallogenic age of gold mineralization has always been one of the interesting research topics as well as unraveling the source of lead. Lead isotope studies have been extensively carried out to determine the age of rocks and minerals, examine geological processes and constrain the source of the metals [9–12], and provide insights into ore genesis [13–18]. Isotopic ratios vary through time for Pb^{206}/Pb^{204}, Pb^{207}/Pb^{204}, and Pb^{208}/Pb^{204}, and Pb isotope studies can be useful in metallogenic research. These isotopes are also helpful for understanding the source of minerals and fluids.

Pyrite (FeS_2) is the most abundant sulphide mineral in the crust, occurring in various geological environments [19–21]. It is also a common sulphide mineral in several ore deposits [16,22]. Some of the elements that can be found in the structure of pyrite are Au, Ag, Cu, Zn, Co, Ni, As, Sb, Se, Te, and Hg [20]. These elements may be present in economical amounts in pyrite. Pyrite can also contain solid inclusions of sulphide,

sulfosalts, and native metals [23]. Gold deportment in pyrite elemental maps can be a clue to knowing the location, distribution (i.e., elemental zoning pattern or internal texture inside pyrite), and timing of gold deposition. This may play a key role in the assessment of mineral processing and extraction.

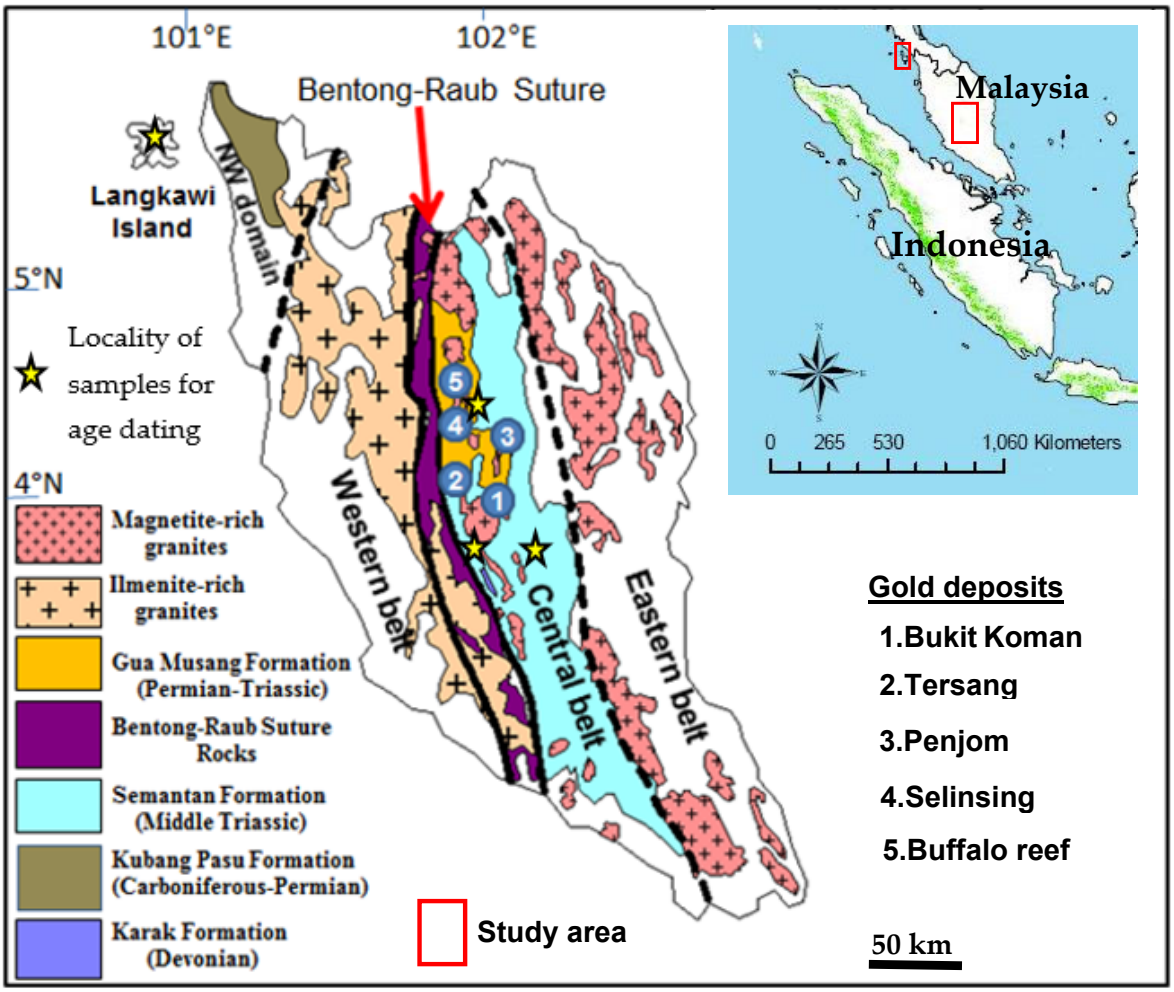

Figure 1. Geological map of the Malaysian Peninsular showing the NW domain, the Western belt, the Central belt, and the Eastern Belt (modified from [7]). Note the locations of Tersang (2) and Selinsing (4) gold deposits for this research work. The two blue boxes in the index map indicate that both the Central belt and Langkawi Islands are study areas. Samples were collected from both areas. The star on the Langkawi Islands represents the sample locality for GRL-0313. The star next to the Selinsing gold deposit is where samples GM-0113 and GM-0213 were collected. Southwest of Bukit Koman is where BE-11513 was collected. Southeast of Bukit Koman in the Semantan Formation is where samples ME-6512 and ME-11813 were taken from. Gold mining is particularly concentrated in the Permo-Triassic Gua Musang Formation as this formation contains sulphide mineralization. Common sulphide minerals found in the Gua Musang rocks are pyrite, galena, sphalerite and chalcopyrite. Pyritic mineralization is also found in the Semantan Formation and granitoid rocks.

The purpose of this study is the following: (1) document age of crystallization of granitoids; (2) estimate the timing of gold mineralization based on Pb isotope composition of ore-related pyrites; (3) discuss lead isotopic compositions of selected pyritic black shale samples at and away from existing sediment-hosted/orogenic gold deposits; (4) compare the lead isotopic composition of host rock-hosted pyrite in surrounding gold deposits to that of K-feldspar from granitoids; (5) determine the trace element composition of pyrite hosted in granitoids.

2. Regional and Tectonic Setting

Malaysia is characterized by the presence of three tectonic belts: the Western Belt, the Central Belt, and the Eastern Belt (Figure 1). The Central Belt is transected by the Bentong-Raub Suture Zone, which is the boundary between Sibumasu and the East Malaya Terrane (Indochina) and represents the location of the closure of the Palaeo-Tethys Ocean [24–26].

This suture zone is characterized by a mélange zone ranging in width from 13 to 20 km [27]. This zone also hosts ribbon-bedded cherts and schists containing elongated blocks of serpentinized mafic and ultramafic rocks. In addition, the formation of the Bentong-Raub Suture Zone was probably coeval with the emplacement of major faults that were conduits for most of the mineralizing fluids.

The Western Belt occupies the western part of Malaysia and has abundant tin deposits. It is characterized by Early Palaeozoic continental margin sequences, Late Palaeozoic platform carbonates, Triassic platform carbonates and deep basinal clastic sequences, and Jurassic-Cretaceous continental deposits. This Belt is also associated with the Main Range magmatic rocks which are large plutons that extend to the southern part of Peninsular Thailand and central Thailand. Tin deposits in this belt are associated with granites that contributed 55% of the historic tin production of Southeast Asia [28].

The northwestern domain lies in the northwestern region of Peninsular Malaysia and comprises the offshore Langkawi Islands and the Carboniferous-Permian Kubang-Pasu Formation as well as the predominant ilmenite-series, S-type granitoids. At the Langkawi Islands, the Machinchang and Singa Formations are exposed. The samples of pyrite in the sandstone and black shales of these formations were collected, including granitic specimens.

The Central Belt comprises mainly Permo-Triassic metasediments, and deep-to-shallow marine sedimentary rocks [3,7,29,30]. Within the Central Belt crop out the Gua Musang Formation, the Semantan Formation, the Karak Formation (Figure 1) as well as the Bentong-Raub rocks, in which are found the BRSZ Unit 1 and 2 [7].

This belt also hosts limestones with intermediate-to-felsic volcanic and volcaniclastic rocks, which were deposited in a fore-arc portion of the palaeo-arc basin [1,31–35]. The basement of the Central Belt consists of a Carboniferous-Permian sequence composed of felsic-to-intermediate volcanic rocks, limestone, shale and subordinate sandstone, siltstone, and conglomerate [36]. Major orogenic gold deposits such as the Penjom, Tersang, Raub, Bukit Koman gold deposits, and Buffalo Reef gold prospect are located in this belt as shown in Figure 1. The Central Belt is also referred to as the Central Gold Belt as it hosts several gold deposits.

The formation of the Bentong-Raub Suture Zone is illustrated in the cross-section shown in Figure 2 below. Figure 2A shows the drifting of Sibumasu from Gondwana. The Palaeo-Tethys Ocean was consumed under the East Malaya down a shallow dipping subduction zone. This subduction event triggered the melting of the mantle and production of granite intrusions into the crust of the Eastern granitoid Belt of Malaysia as well as volcanism. Additionally, the formation of the Bentong-Raub Suture Zone was likely coeval with the emplacement of major faults that were conduits for most of the mineralising fluids. Figure 2B illustrates how the Palaeo-Tethys shrunk as Sibumasu drifted towards East Malaya. This led to the steepening of the subduction zone under East Malaya, accompanied by plutonism and volcanism in the Central Belt. In Figure 2C, Sibumasu collided with the East Malaya terrane during the Upper Triassic, and the subduction zone steepened further and melting occurred. Quartz veins probably formed during the Upper Triassic. The deep water rocks in the Palaeo-Tethys Ocean were fractured inside the Bentong-Raub Suture Zone. Furthermore, plutonism and volcanism progressed through time in the Central Belt of Malaysia.

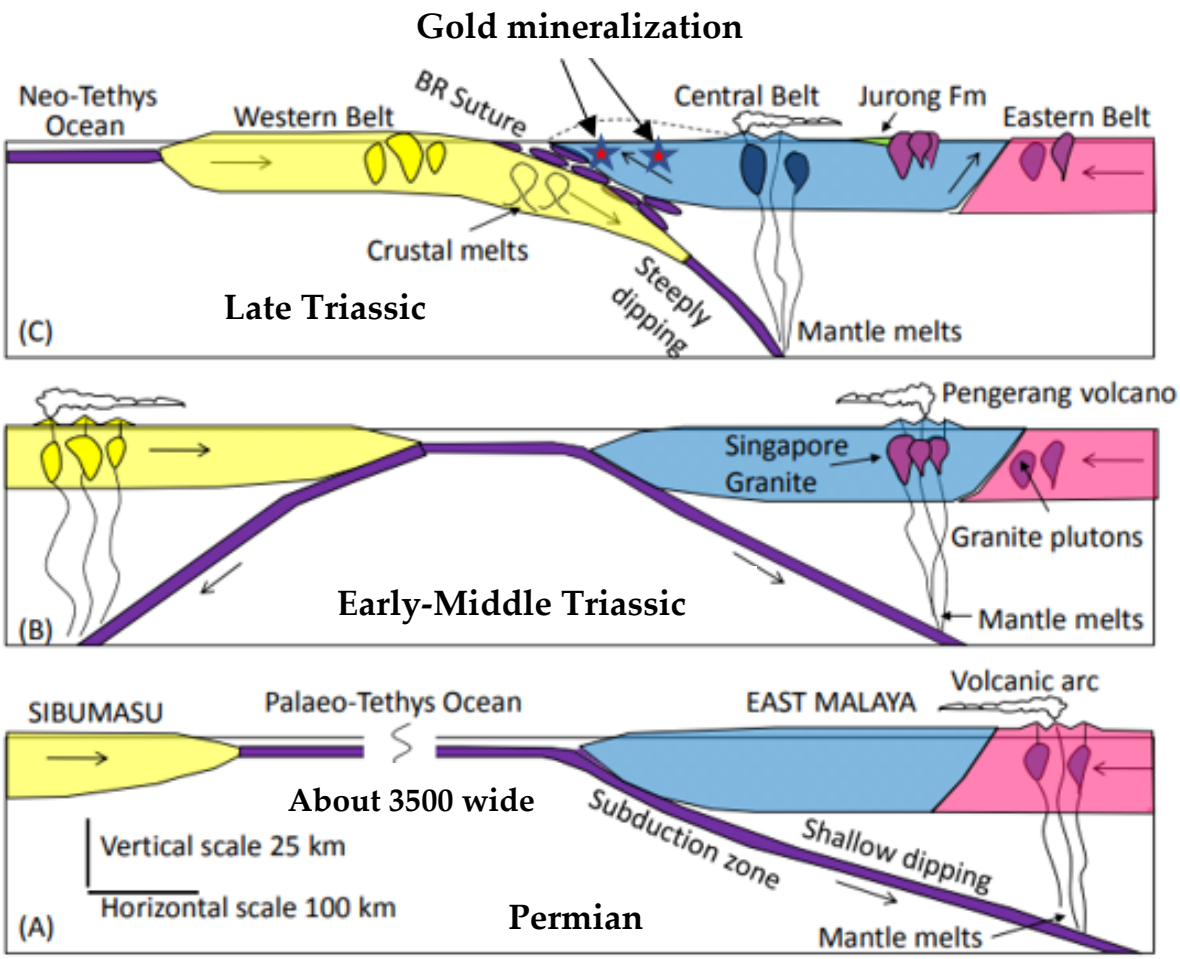

Figure 2. Geodynamics context for the formation of the Bentong-Raub (BR) Suture Zone in relation to the closure of the Paleo-Tethys Ocean (Modified from [37]). In late Triassic, several magmatic events favored the emplacements of S- and I-type granites across the suture zone. The collision of the Sibumasu and East Malaya blocks occurred in Late Triassic (200–230 Ma) to form the Bentong-Raub Suture Zone. Note (**A**) Permian (290–250 Ma). (**B**) Early-Middle Triassic (250–230 Ma). (**C**) Late Triassic (230–200 Ma).

The Eastern Belt is characterized by deformed Late Palaeozoic sequences, which are overlain unconformably by Late Permian continental conglomerate and Jurassic-Cretaceous continental deposits. The age of the Eastern Belt granites ranges from Permian to Triassic and these ages are mostly young (220–240 Ma) towards the Bentong-Raub Suture Zone, and close to 200 Ma adjacent to the suture. The magmatic rocks in this belt cover a wide compositional range from biotite granite to hornblende-biotite granite/granodiorite and diorite-gabbro [28].

In addition, this belt includes a suite of shoshonitic trachyte in the Segamat area (Johor) which has been dated by K/Ar dating and returned the age of 62 Ma [38].

The Eastern Belt plutons consist of 87Sr/86Sr initial ratio (less than 0.712) for biotite or hornblende-biotite-bearing I-type igneous rocks with Triassic Rb-Sr ages. I-type magmatic rocks are typical of modern-day Andean-type active margins where oceanic plates are subducted under continental margins or islands arcs producing andesite volcanoes. Additionally, ref. [39] obtained U-Pb zircon ages of ~260 Ma and ~220 Ma (i.e., Upper Permian to Middle Triassic) from the I-type granitoids in this belt. This belt is also characterized by magmatism associated with the subduction of an ancient ocean (Palaeo-Tethys Ocean) under the Central and Eastern Belts. Ref. [40] documented that both I-type and S-type granitoids are present in this belt.

3. Ore Deposits

The Selinsing and Tersang gold deposits which lie east of the Bentong-Raub Suture Zone were selected to address the aims of this study. The Selinsing gold deposit is in the northwest of Pahang and approximately 50 km north of Raub Town (Figure 3). The host rocks consist of phyllite, calcareous black mudstone, tuffaceous siltstone, and sandstone of the Permo-Triassic age. The sedimentary host sequence has undergone low-grade metamorphism. The deposit is characterised by a series of auriferous quartz veins and stockwork of quartz veinlets. Refs. [3,41] report that gold mineralization at Selinsing is controlled by shearing and faulting. The structures are in the form of pinch and swell quartz veins, and stockwork of quartz stringers, which are found in the host rocks.

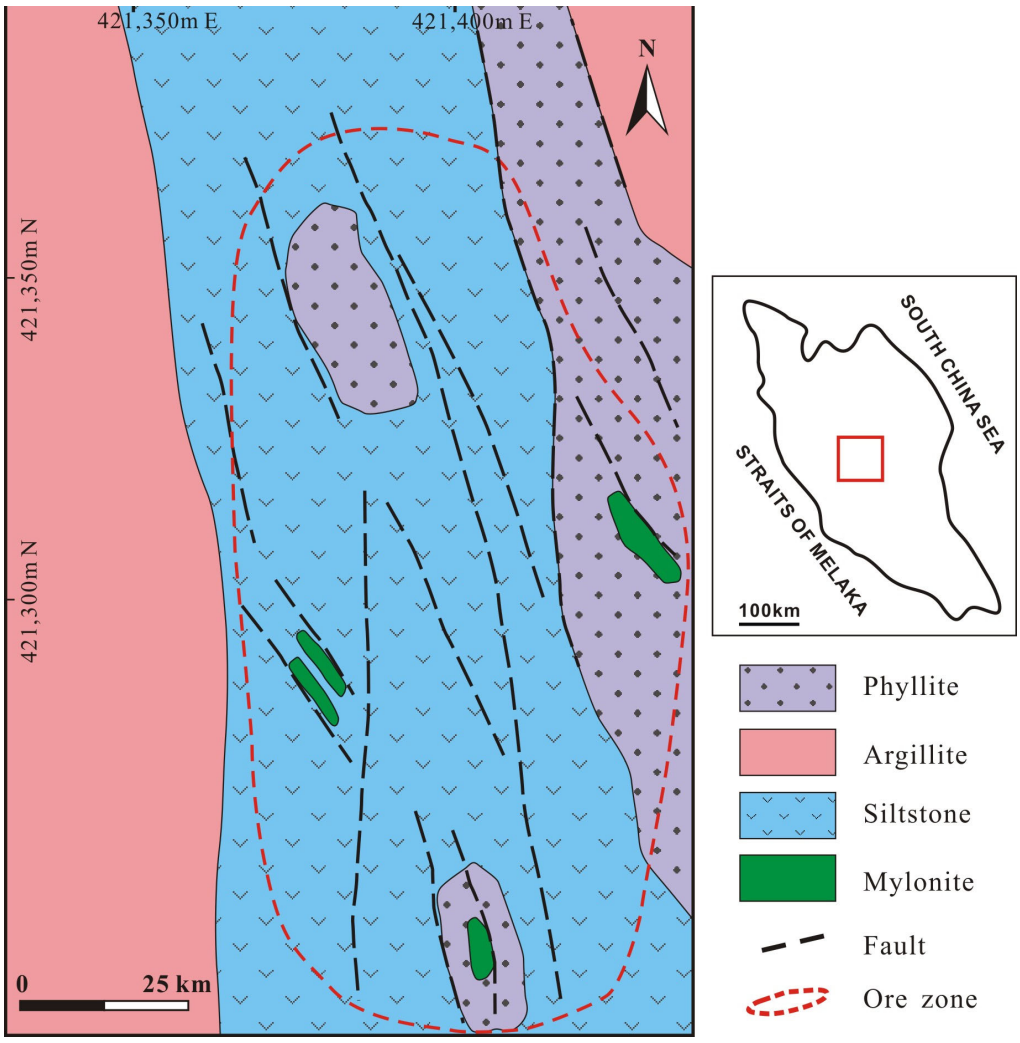

Figure 3. Geological map of the Selinsing gold deposit (Modified from [3]).

Gold mineralization occurs in a 30–50 m thick shear zone dipping towards the mine grid east at 55°–75°. A dip-slip reverse thrusting had caused compression from the east crosscutting the stratigraphy. Tectonic rock types, such as cataclasite and mylonite representing ductile and brittle shear zones are also present. Most importantly, gold mineralization is in the form of fine gold particles commonly associated with arsenopyrite and galena. Patches of electrum were also found associated with galena [5].

The Tersang gold deposit is located approximately 20 km North of Raub Town along the Bentong-Raub Suture Zone. The main lithologies consist of grey sandstone and breccia, which are crosscut by a massive rhyolite dyke in the fault zone (Figure 4). The rhyolite body measures approximately 600 m long and 400 m wide in the central and northern part of the deposit. The rhyolite branches out in the form of sills along bedding planes in the sandstone layers. Samples of the pyrite grains were collected from black shales and sandstones. Several sites were visited to collect samples of granites, black shales, tuffs, and sandstones.

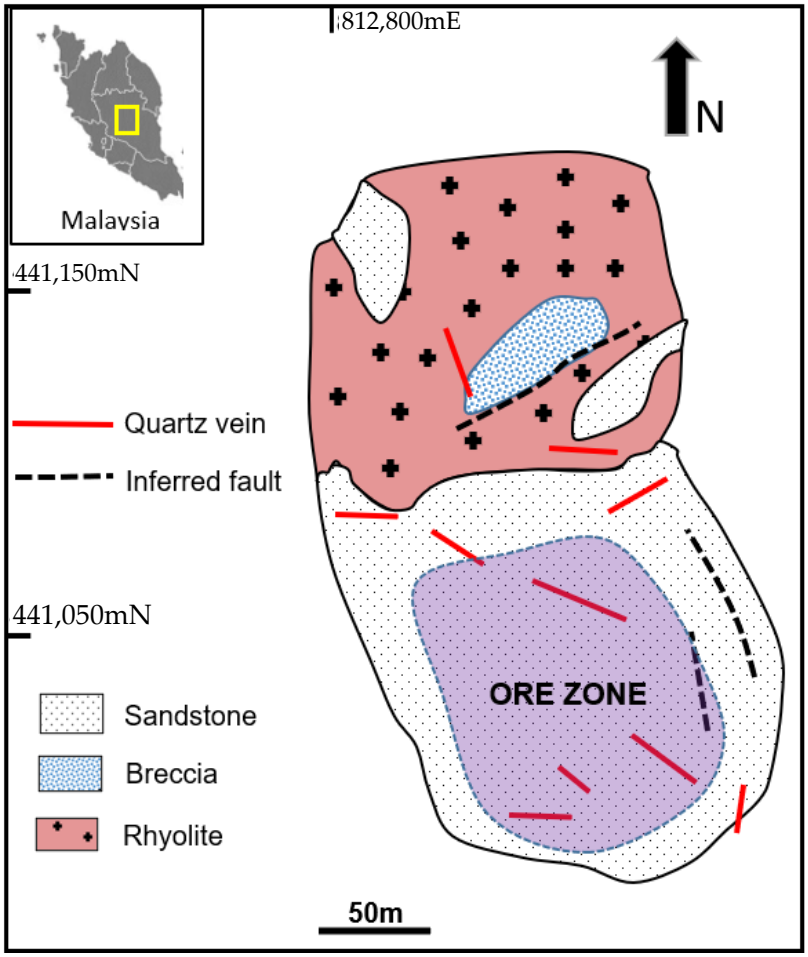

Figure 4. Geological map of the Tersang gold deposit (Modified from [3]).

4. Materials and Methods

4.1. Pyrite Samples

In this study, hand specimens came from the Singa Formation, Semantan Formation, and BRSZ Unit 1 (Figure 5), as well as magmatic rocks (Figure 6).

Pyrite samples were also collected from the Selinsing, Tersang, and Penjom gold deposits. The Machinchang pyrite crystals are 100–200 µm across and they contain inclusions of rutile ranging in size from 50 to 100 µm. The Singa pyrite crystals are subhedral and mostly coarse grains ranging in size up 2 mm. The Semantan pyrites are framboids that are less than 20 µm across. The BRSZ Unit 1 pyrite crystals are subhedral in shape and their size varies up to 60 µm. Igneous-rock hosted pyrite crystals are subhedral to euhedral with sizes that range up to 1.5 mm (Figure 7).

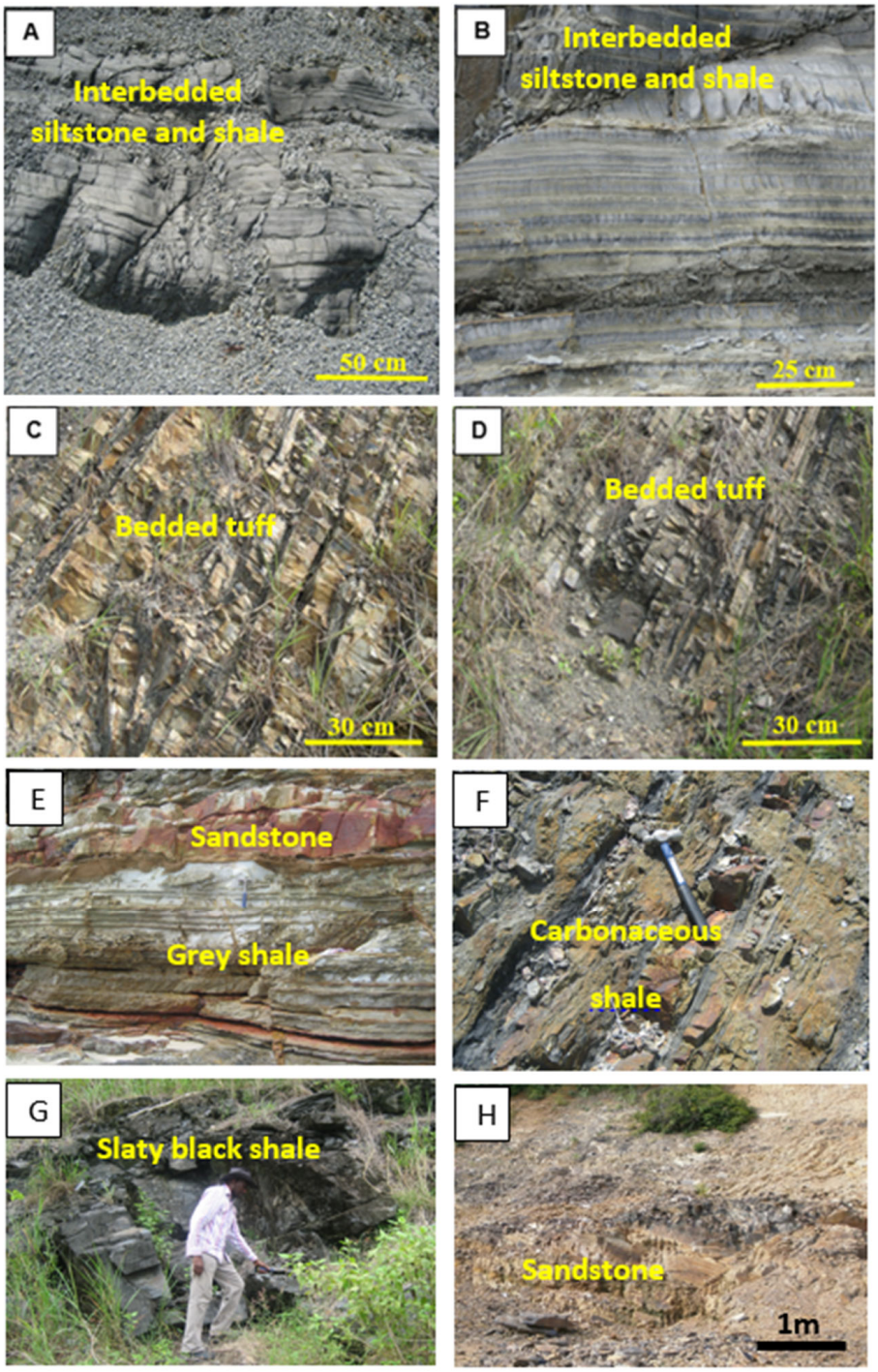

Figure 5. Outcrop photographs of selected formations from where pyrite samples were collected in the field. (**A**) Interbedded black tuffaceous siltstone and black shales from the Semantan sedimentary environment. (**B**) Close-up view of the turbidite sequence. (**C**) Coarse-grained bedded tuff. (**D**) Fine-grained bedded tuff. Field mapping has shown that the Semantan Formation is made up of interbedded tuffaceous siltstone (1–3 cm thick layers) and tuffaceous black shales (up to 2 cm thick layers). The shales contain organic matter laminations (2–3 mm). (**E**) Interbedded sandstone and grey shale of the Machinchang Formation. (**F**) Carbonaceous black shales with siltstone laminations of BRSZ Unit 1. (**G**) Slaty black shale of the Singa Formation. (**H**) The sandstone of the Singa Formation.

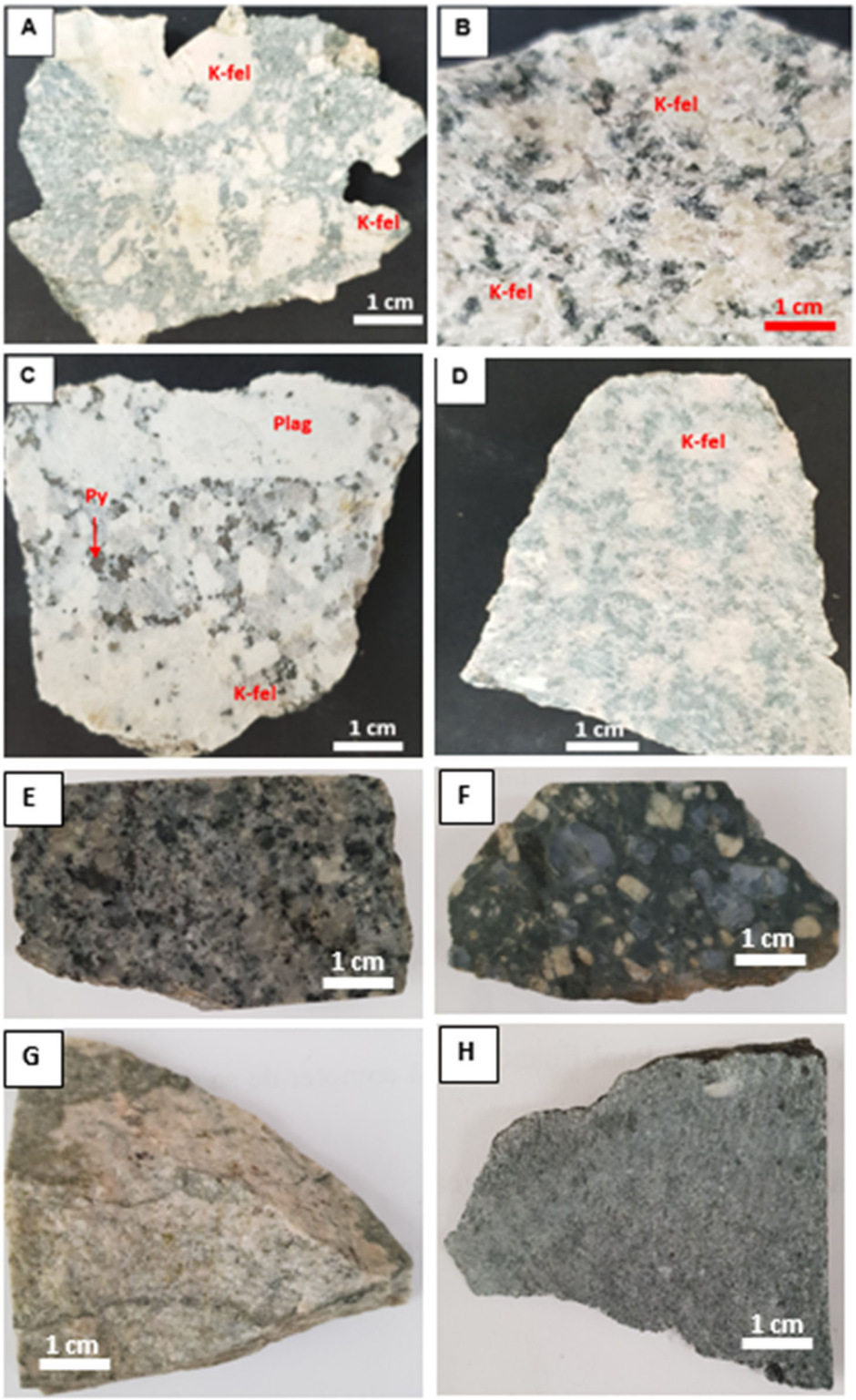

Figure 6. Selected granitoid rock samples from Malaysia on which the Pb isotope of K-feldspar was undertaken. (**A**) Hand specimen of megacrystic granite from the Bentong area (sample: BE-11513). (**B**) Granite GM-0113. (**C**) Granite GRL0313. (**D**) Granite GM0213. Samples that contain pyrite used to determine Pb isotope composition are hand specimens as displayed in images (**E**) Granodiorite (sample BG-0313); (**F**) Diorite with phenocrysts of plagioclase and quartz; (**G**) Rhyolite and (**H**) Dolerite. Plag = Plagioclase, K-fel = K feldspar, Py = Pyrite.

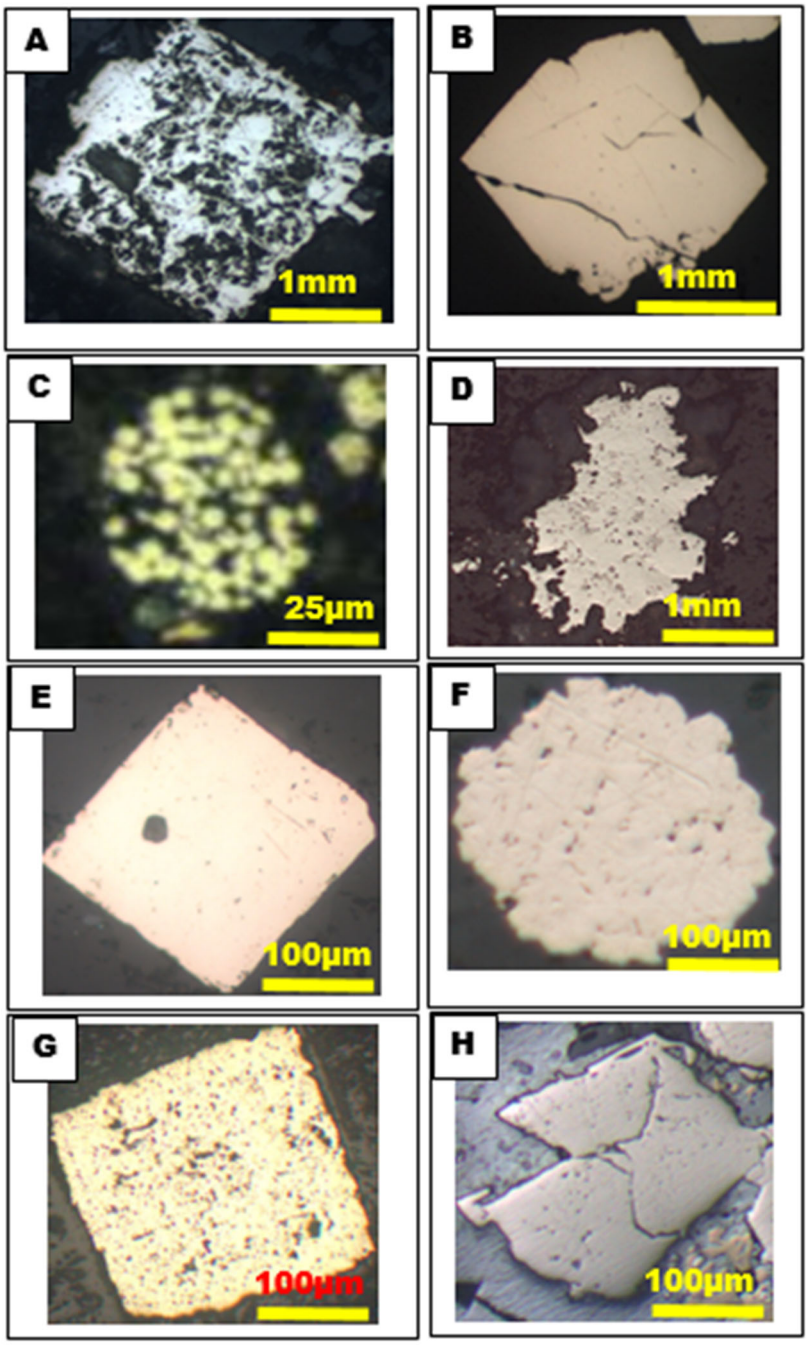

Figure 7. Photomicrographs of pyrite crystals from selected formations. (**A**) Euhedral pyrite from the Machinchang Formation (LA-3312B). (**B**) Singa Formation pyrite (LA-5312B). (**C**) Sedimentary pyrite from the Semantan Formation (ME-5912). (**D**) Subhedral pyrite from the BRSZ Unit 1 (BE-2412B). (**E**) Pyrite from Ilmenite-series, igneous rock (BG-0313). (**F**) Selinsing pyrite (SEL-R009-7). (**G**) Tersang pyrite. (**H**) Penjom pyrite (PEN-R16A).

4.2. U-Pb Zircon Dating

Approximately 100 g of rock was repeatedly sieved and crushed in a Cr-steel ring mill to a grain size <400 micron. Non-magnetic heavy minerals were then separated using a gold pan and a Fe-B-Nd hand magnet. The zircons were handpicked from the heavy mineral concentrate under the microscope in cross-polarised transmitted light. The selected crystals were placed on double-sided sticky tape and epoxy glue was then poured into a 2.5 cm diameter mould on top of the zircons. The mount was dried for 12 h and polished using clean sandpaper and a clean polishing lap. The samples were then washed in distilled

water in an ultrasonic bath. The standard procedure for the Laser ICP-MS zircon dating is performed on an Agilent 7500cs quadrupole ICPMS with a 193 nm Coherent Ar-F gas laser and the Resonetics M50 ablation cell at CODES, University of Tasmania.

The downhole fractionation, instrument drift, and mass bias correction factors for Pb/U ratios on zircons were calculated using two analyses on the primary (91,500 standard of [42]) and one analysis on each of the secondary standard zircons (Temora standard of [43,44]) analysed at the beginning of the session and every 12 unknown zircons (roughly every 1/2 h) using the same spot size and conditions as used on the samples. Additional secondary standards (The Mud Tank Zircon of [45]) were also analysed. The correction factor for the $^{207}Pb/^{206}Pb$ ratio was calculated using three large spots of NIST610 analysed at the beginning and end of the day and corrected using the values recommended by [46]. Each analysis on the zircons began with a 30 s blank gas measurement followed by a further 30 s of analysis time when the laser was switched on. Zircons were sampled on 32-micron spots using the laser at 5 Hz and a density of approximately 1.5 J/cm^2. A flow of He carrier gas at a rate of 0.6 litres/minute carried particles ablated by the laser out of the chamber to be mixed with Ar gas and carried to the plasma torch.

Elements measured included ^{49}Ti, ^{96}Zr, ^{146}Nd, ^{178}Hf, ^{202}Hg, ^{204}Pb, ^{206}Pb, ^{207}Pb, ^{208}Pb, ^{232}Th, and ^{238}U, with each element being measured sequentially every 0.16 s with longer counting time on the Pb isotopes compared to the other elements. The data reduction used was based on the method outlined in detail in [14] similar to that outlined in [47,48]. Element abundances on zircons were calculated using the method outlined by [49] using Zr as the internal standard element, assuming stoichiometric proportions and using the 91,500 to standard correct for mass bias. For age determination, one hundred and twenty-nine zircon grains were analysed from granitic rocks and volcaniclastic rocks.

4.3. Pb Isotope Analysis

All analyses were conducted at the University of Tasmania using the Laser Ablation Inductively Couple Plasma Mass Spectrometry (LA-ICP-MS) method. The analyses were performed on an Agilent 4500 ICPMS coupled to a New Wave 213 nm solid state laser in a custom made, low volume (3.4 cm^3), barrel-shaped chamber in a He atmosphere. The laser was operated at 5 or 10 Hz using spot sizes between 15 and 110 µm. Data were collected in time-resolved mode with 30 s gas blank measurement followed by 60 s analysis time typically drilling at around ~1 µm s^{-1}. Data deconvolution was performed using custom-made excel-based spreadsheets. Pb isotope analyses were both undertaken on both pyrite and K-feldspar.

In this study, 37 Pb isotope analyses were conducted on pyrite from the Selinsing and Tersang gold deposits. In addition, 49 Pb isotope analyses on pyrite were conducted from selected formations such as BRSZ Unit1 (outcropping in the Bentong-Raub Suture Zone, Machinchang (away from the gold deposits on Langkawi Islands), Singa (away from the gold deposit on Langkawi Islands), and Semantan formations (south of the gold deposits). There were 36 Pb isotope analyses carried out on K-feldspar from granitic rocks that crop out in the suture zone and in the vicinity of the Selinsing and Tersang gold deposits. The reason for covering both areas was to see if there was any variation in the Pb isotope in the K-feldspar crystals.

4.4. Pyrite Trace Element Geochemistry

The trace element contents in the selected pyrite samples were analyzed by Laser ablation inductively coupled mass spectrometry (LA-ICP-MS) at the Centre for Ore Deposit and Earth Sciences (CODES), University of Tasmania. The instrument combined a Resolution 193 nm excimer laser, mixed with an Agilent 7700x ICP-MS. The spot sizes used were 10, 15, 20, and 22 µm depending on the size of the pyrite grain. A total of 29 elements were analyzed on pyrite grains including: Na, Mg, Al, Si, K, Ca, Ti, V, Cr, Mn, Fe, Co, Ni, Cu, Zn, As, Se, Mo, Ag, Sb, Te, W, Pt, Au, Hg, Tl, Pb, Bi, and U. The signal from the carrier gas with no ablation was regularly acquired to correct for instrumental background. The following

reference materials were used for primary calibration and assessment of elemental contents: STDGL2b2 [50] and STDGL3 [51,52] for siderophile and chalcophile elements, GSD-1G [53] for lithophile elements, and PPP-1 pyrite for sulfur [54].

4.5. Magnetic Susceptibility

All igneous rock samples collected were submitted for testing for their magnetic susceptibility properties. This was important to establish the batches that had S- or I-type affinity. The magnetite and ilmenite series granite classification were determined by the magnetite content of granitic rocks which could be characterized by the magnetic susceptibility (MS) which indicates the oxygen fugacity of the granitic magma.

The magnetic susceptibility of the granitic rocks ranged from 0.08 $\times$ 10^{-3} SI to 18.58 $\times$ 10^{-3} SI, corresponding respectively to ilmenite series (<3 $\times$ 10^{-3} SI; oxidized type) and magnetite series (>3 $\times$ 10^{-3} SI; reduced type) granite [55,56]. In this study, 37 magnetic susceptibilities (MS) were measured during fieldwork on the margins of the suture zone, in the vicinity of the gold deposits, and on Langkawi Islands in order to discriminate S- from I-type granitic rocks.

5. Results

5.1. U-Pb Zircon Dating of Granite and Volcaniclastic Sediments

Six igneous rock samples that crop out in the Central Belt and Langkawi Islands were dated using the U-Pb zircon dating. Cathodoluminescence imaging shows that the zircon crystals were of variable shape and size; however, the majority were elongated or acicular, partly broken, and display oscillatory growth zones for the granitoids from the Gua Musang area. The crystals are mostly subhedral in shape and 25–125 µm in length (Figure 8).

Figure 8. Cathodoluminescence (CL) images of zircon grains from the Gua Musang area, Malaysia. The round feature represents the position of the laser craters.

Zircon grains from the Bentong area and the Langkawi Islands show growth zones and a few display rims. Some have rounded edges and are pitted (Figure 9). They are 30–170 µm in length. In addition, zircon grains from the Semantan tuffaceous sandstones are subhedral and show both sharp and rounded edges.

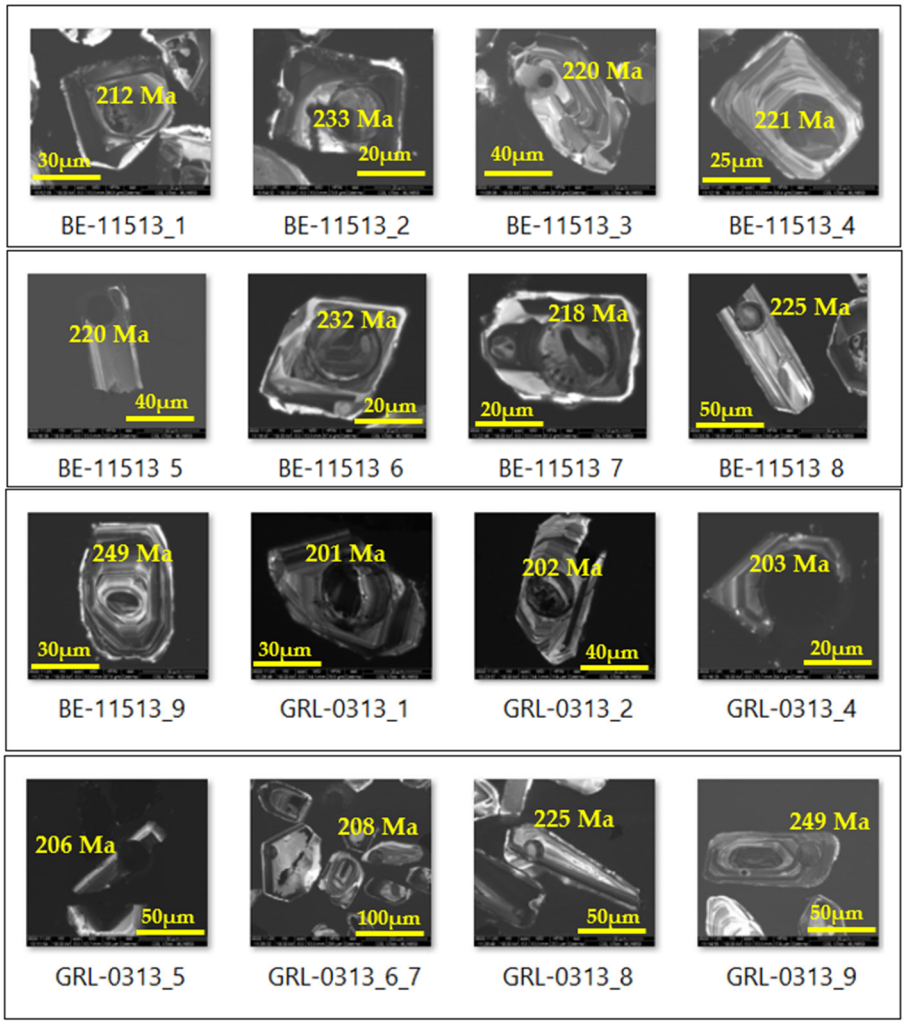

Figure 9. Cathodoluminescence (CL) images of zircon grains from the Bentong area and Langkawi Islands, Malaysia. The round feature represents the position of the laser craters.

The zircon grains are 40–150 µm in length (Figures 9 and 10). The crystallization ages of the granites are shown in Figures 9 and 10. From the Gua Musang granites found in the vicinity of the Selinsing gold deposit, 89 zircon crystals were analyzed.

Based on these analyses, the following ages were obtained: 205.6 ± 3.2 Ma; MSWD = 1.7 and 204.1 ± 4.7 Ma; MSWD = 1.5 as shown in Figure 11A–D. U-Pb zircon dating of the Langkawi granite indicates an age of 208 ± 2.5 Ma; MSWD = 2.0 and the granite is close to the Bentong-Raub Suture zone. Granitoid rocks (samples GM-0113 and GM-0213) from the Gua Musang area have Th/U ratios ranging from 0.2 to 1.3. The one (sample BE-11513) located in the Bentong-Raub Suture Zone has a Th/U ratio between 0.7 and 2.2. The sample GRL-0313 has a Th/U ratio that varies between 0.09 and 3.43. Those located in the Semantan Formation have Th/U ratios ranging from 0.04 to 1.17.

Forty zircon crystals were analyzed for the tuffaceous sandstone returned a Middle Triassic (Ladinian) age of 231.6 ± 3.6 Ma (MSWD = 1.3) and 233.1 ± 1.6 Ma (MSWD = 0.97) as shown in Figure 11E,F. MSWD data represent the Mean Square of Weighted Deviates. Data of U-Pb zircon dating are shown in Table S1.

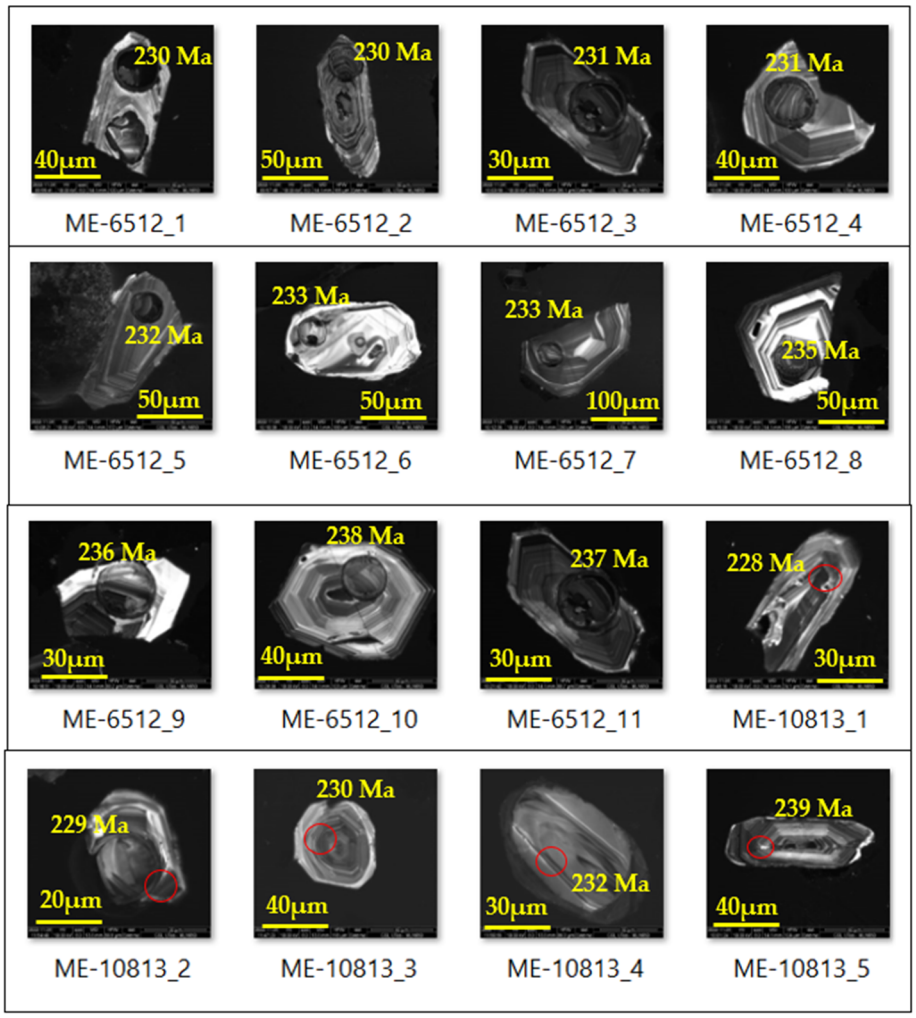

Figure 10. Cathodoluminescence (CL) images of zircon grains from the Semantan area, Malaysia. The round feature represents the position of the laser craters.

5.2. Lead Isotope from K-Feldspar

The Pb isotope compositions of K-feldspar of these low-magnetic susceptibility granitoids are given in Table S2. All K-feldspar-bearing granitic rocks from the Gua Musang area have the following Pb isotope compositions: $^{207}Pb/Pb^{206}$: 0.81–0.88; $^{208}Pb/Pb^{206}$: 2.04–2.14; $^{206}Pb/Pb^{204}$: 17.73–19.52; $^{207}Pb/Pb^{204}$: 14.99–17.14; $^{208}Pb/Pb^{204}$: 37.65–41.37 and $^{206}Pb/Pb^{238}$: 5.14–693.51. In contrast, those from the Bentong-Raub area close to the eastern side of the suture zone have the following Pb isotope compositions: $^{207}Pb/Pb^{206}$: 0.82–0.85; $^{208}Pb/Pb^{206}$: 2.07–2.14; $^{206}Pb/Pb^{204}$: 18.53–19.21; $^{207}Pb/Pb^{204}$: 15.39–16.09; $^{208}Pb/Pb^{204}$: 38.75–40.36 and $^{206}Pb/Pb^{238}$: 3.30–2755.42. The $^{206}Pb/Pb^{238}$ shows extended values compared to the other ratios (Figure 12A).

Overall, the granites show two different Pb isotope compositions; one (the red polygon on the average crust line) which has low $^{206}Pb/^{204}Pb$ ratios (far from the gold deposits), and the other (the red polygon near the upper crust line—Figure 12A) which has slightly high $^{206}Pb/^{204}Pb$ ratios.

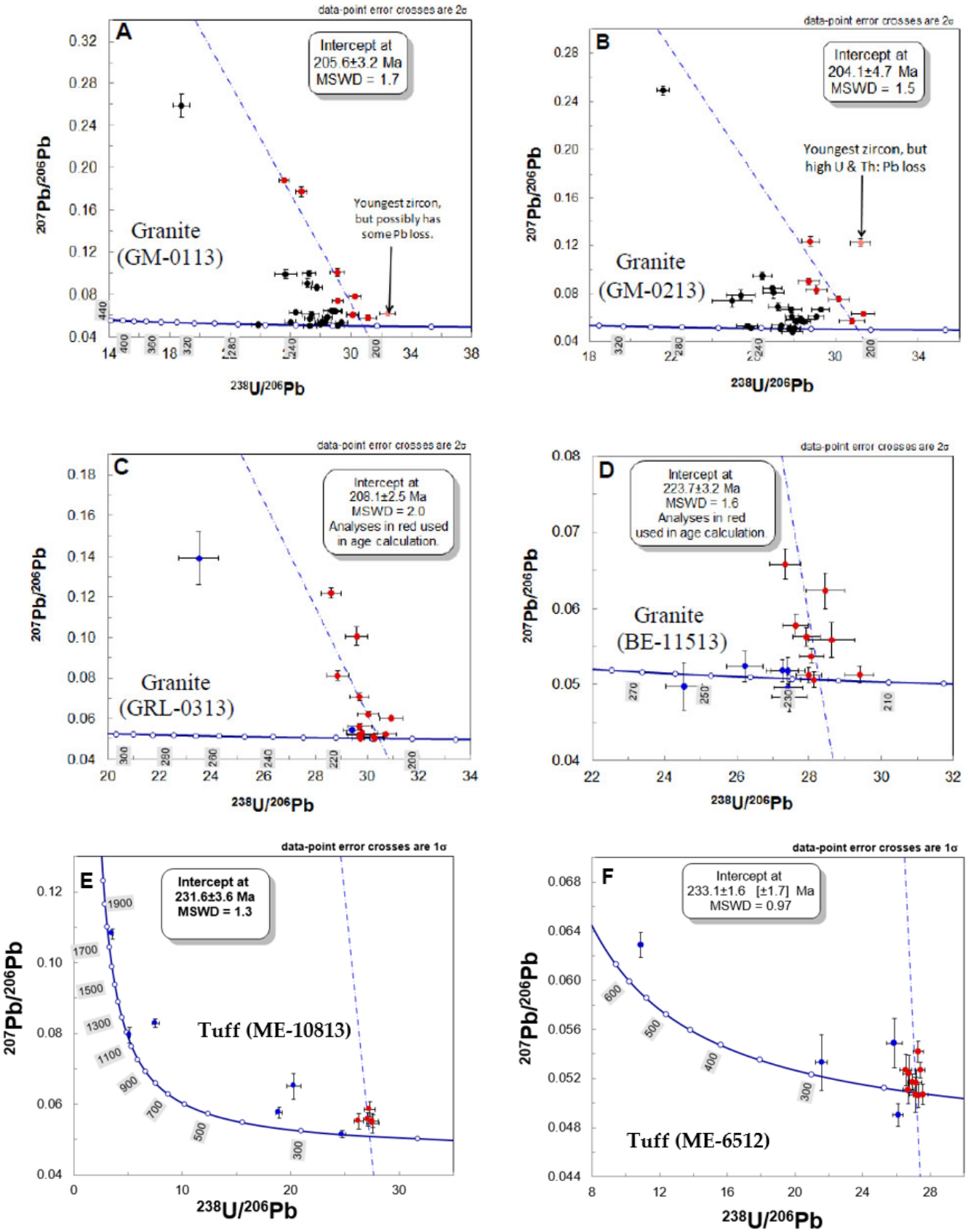

Figure 11. U-Pb dating of granite and tuff samples outcropping in the Central Belt. All the plots indicate the crystallization age of the granite. (**A**) U-Pb zircon dating of the Gua Musang granite in the vicinity of the Selinsing gold deposit. (**B**) U-Pb zircon dating of the Gua Musang granite in the

vicinity of the Selinsing gold deposit. (**C**) U-Pb zircon dating of the Langkawi granite. (**D**) U-Pb zircon dating of the granite close to the Bentong-Raub Suture zone. (**E**,**F**). U-Pb inverse concordia plot of Semantan Tuffs close to the Bentong-Raub Suture Zone. Note Figure A shows overlapping numbers of the blue line across the X-axis as most analyses have $^{207}Pb/^{206}Pb$ ratio between 0.04-0.012 along Y-axis. The progression on the X-axis is 14, 18, 22, 26, 30, 34 and 38. The same applies on Figure (**B**).

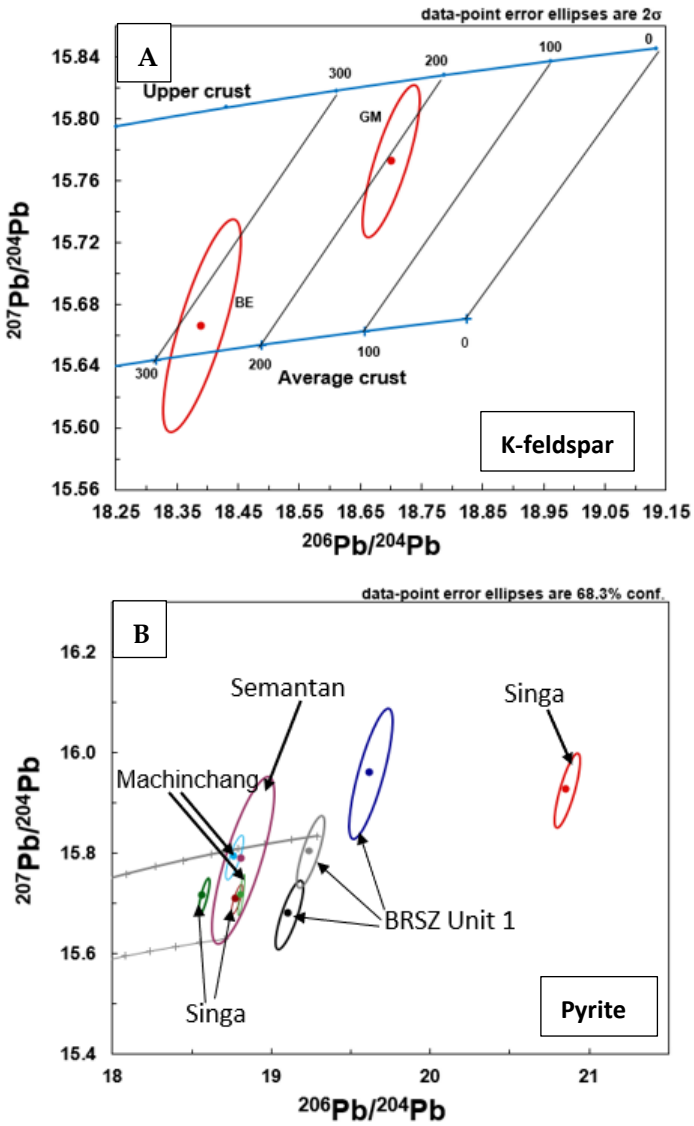

Figure 12. Lead isotope composition. (**A**) Lead isotope composition on K-feldspar from selected ilmenite-series granitic rocks cropping out in the Gua Musang (GM) and the Bentong area (BE). Red ellipses represent the two populations. The Gua Musang area is where most orogenic gold deposits such as Selinsing, and Tersang deposits are found. This graph was adapted from the model of [57]. The BE data plot is close to the average crust which is referred to as the subduction line. However, the GM data cluster below but close to the upper crust line. The 200 Ma Pb-Pb model age line transects the ellipse for the GM data; whereas the 300 Ma Pb-Pb model age line appears off-trend across the ellipse of the BE data. The results of the Pb isotopic composition in K-Feldspar are shown in Table S2. Abbreviation Fm means formation. (**B**) Pyrite Pb isotope composition on pyrite from the Machinchang, Semantan, BRSZ Unit 1, and Singa Formations. The data represent the background Pb isotopic composition compared to the Pb isotopic composition of ore-hosting pyrites at the Selinsing and Tersang gold deposits. The results of the Pb isotopic composition in pyrite are shown in Table S3.

5.3. Pyrite Pb Isotope Composition

Prior to interpretation, the pyrite Pb isotope compositions were filtered to remove outliers (MSWD > 2.5, $^{206}Pb/^{204}Pb$ precision > 0.5%, and $^{206}Pb/^{238}U$ > 5). The Pb isotope compositions of the pyrite grains from the Machinchang, Singa, Semantan, BRSZ Unit 1, granite, and Gua Musang Formations are shown in Figure 12 and results are given in Table S3. The Pb isotope compositions indicate that there is considerable variation in the Pb isotopic composition of the pyrite grains analyzed.

The Machinchang and Semantan pyrites tend to be less radiogenic with low $^{206}Pb/^{204}Pb$ ratios than the BRSZ Unit 1 pyrite from the Bentong-Raub Suture Zone which have high $^{206}Pb/^{204}Pb$ ratios (Figure 12B). The variation in Pb isotopic composition from each sample is likely related to the in situ decay of U and Th but the remainder corresponds to initial isotopic differences during the crystallization of pyrite. The Singa Formation contains pyrites with two different compositions: one is similar to the Machinchang and Semantan but slightly lower in $^{207}Pb/^{204}Pb$, and the other is much more radiogenic than the BRSZ Unit 1 pyrite (Figure 12B).

The Pb isotope plots for the ratio $^{206}Pb/^{204}Pb$ versus $^{207}Pb/^{204}Pb$ for pyrite from both the Selinsing and Tersang gold deposits are presented in Figure 13. The Selinsing pyrite core and rim results indicate variable Pb isotope compositions. For instance, the Selinsing pyrite rims are more radiogenic than the Selinsing pyrite cores. The Tersang pyrite core and rims have consistent values that are similar to the least radiogenic of the Selinsing pyrite cores.

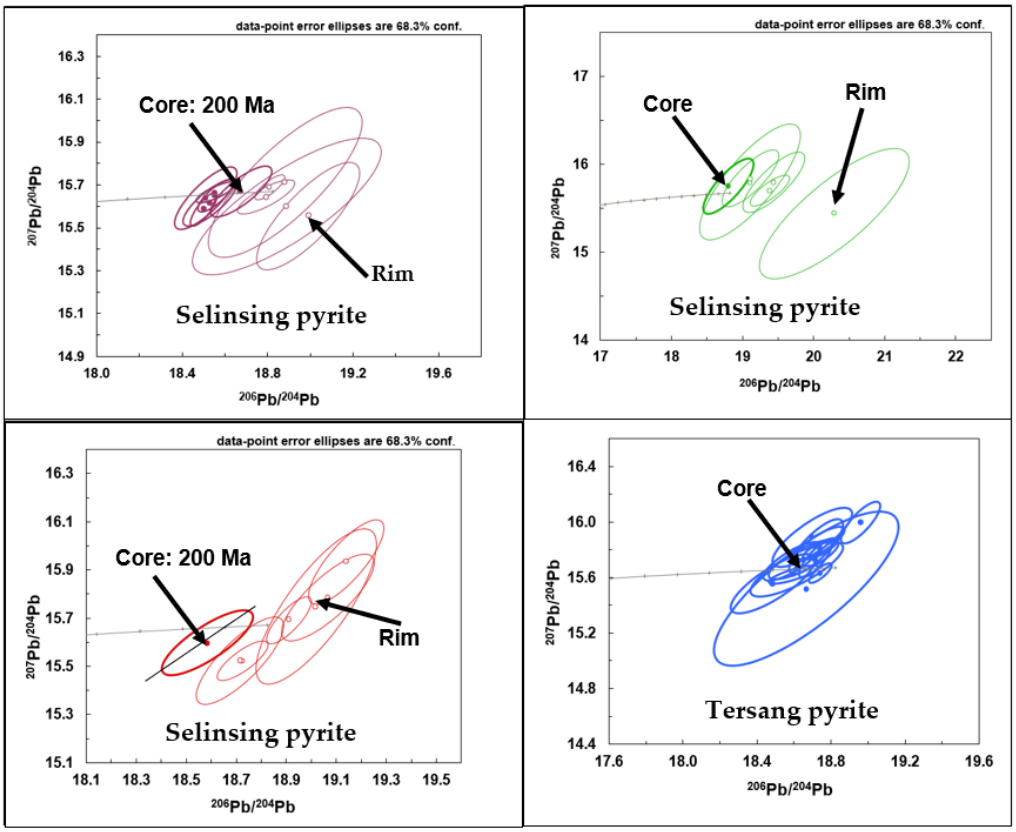

Figure 13. Laser ablation ICP-MS analysis of $^{206}Pb/^{204}Pb$ and $^{207}Pb/^{204}Pb$ in pyrite from the Selinsing and Tersang gold deposits. The 200 Ma Pb-Pb model age corresponds to the pyrite core zone for pyrite crystals analyzed for both the Tersang and Selinsing gold deposits.

Research work on pyrite imaging has also shown that there is a strong correlation between Au and Pb in the cores of ore-hosted pyrite crystals (Figure 14) based on pyrite trace element mapping [3]. These pyrite grains are those which were analyzed for their Pb isotope composition in cores and rims. In this study, the results of the Pb isotopes in the pyrite core and rim from the selected gold deposits are presented in Table S4. The plot of Pb^{208} versus Au content in count per second in pyrite from the Tersang and Selinsing gold deposits is shown in Figure 15 and results are given in Table S5. The graph shows that Pb^{208} content in pyrite coupled with gold content can help discriminate pyrite cores from rims.

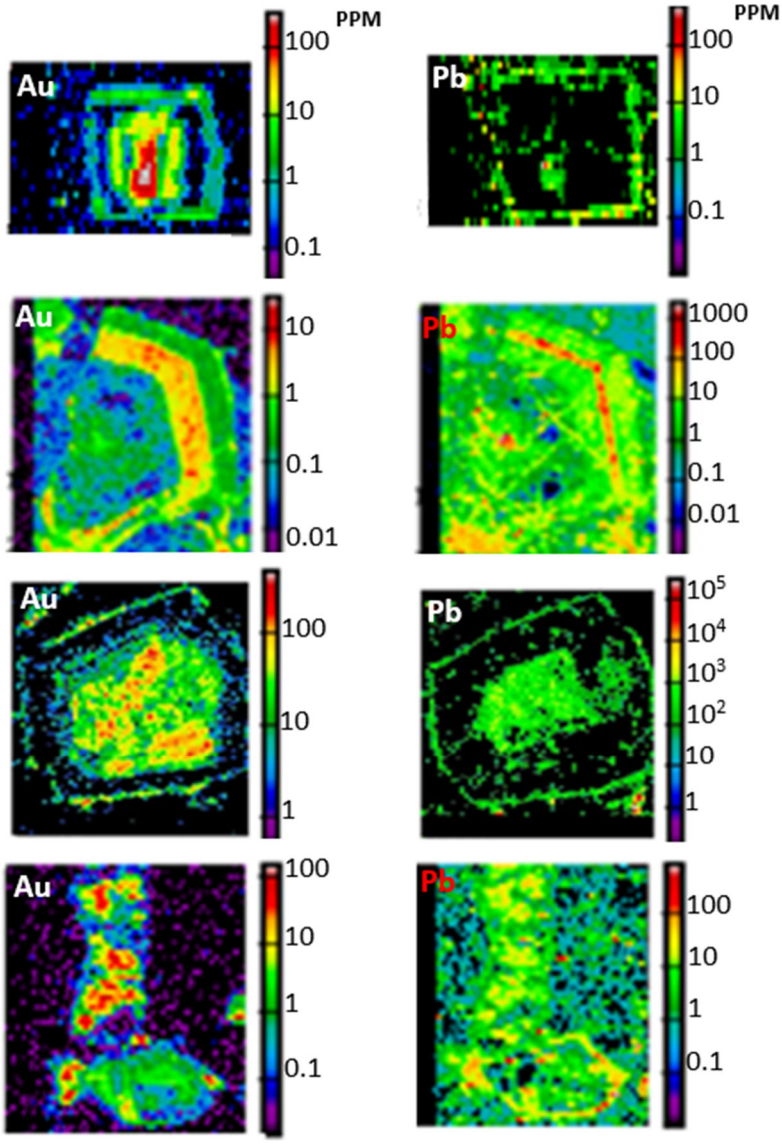

Figure 14. Gold and lead occurrences in pyrite crystals found in black shales from the Tersang and Selinsing gold deposits in Malaysia showing consistent synchronous patterns in the pyrite lattices.

5.4. Trace Elements in Igneous Rock-Hosted Pyrite

Trace elements in the pyrite crystals were analyzed to evaluate their concentration including gold content, as shown in Figure 16. Results indicate that granodiorite-hosted pyrites have elevated trace element contents to more than 1 ppm except for Au and Sn whose values are below 1 ppm. Gold content varies between 2.4 and 88 ppb. Dolerite-hosted pyrites yield elevated contents of Co, Ni, Cu, Zn, As, Se, and Bi more than >1 ppm, whereas Mo, Ag, Cd, Sn, Sb, Au Tl, Pb, and U indicate concentrations below 1 ppm. Gold

content ranges between 0.3 and 655 ppb. Diorite-hosted pyrites have elevated contents of Co, Ni, Cu, Zn, and Se above >1 ppm except for As, Mo, Ag, Cd, Sn, Sb, Au, Tl, Bi and U. Gold content ranges up to 19 ppb. Rhyolite-hosted pyrites display elevated contents of Co, Cu, Zn, As, Se, Pb, and Bi. However, Ni, Mo, Ag, Cd, Sn, Sb, Au, Tl, and U have low contents of less than <1 ppm. Gold content varies between 2.2 and 793 ppb. Results of the trace element composition of magmatic rock-hosted pyrites are shown in Table S6. The relationship between gold and other trace elements are shown in correlation matrix values in Table S7.

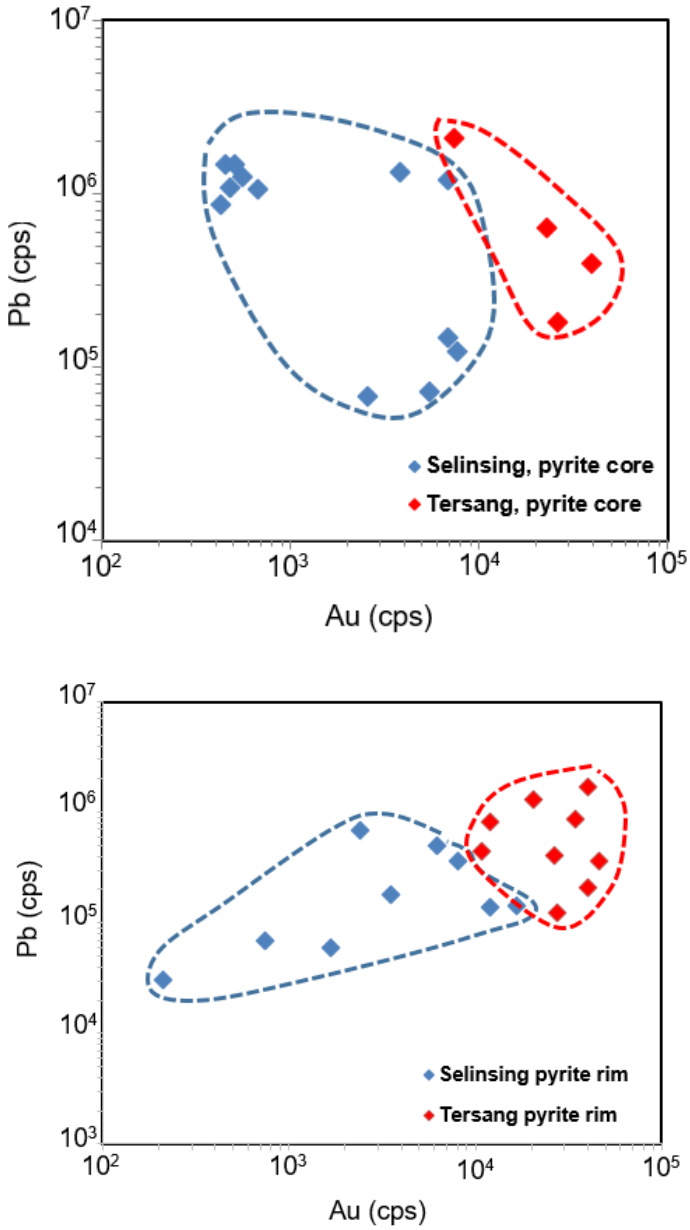

Figure 15. Plot of Pb^{208} versus Au content in count per second in pyrite from the Tersang and Selinsing gold deposits, Malaysia.

5.5. Magnetic Susceptibility

Results indicate that the granitoid rock samples analyzed for lead isotopes in K-feldspar have low magnetic susceptibility (MS). As a whole, the granitoids are mainly ilmenite series (S-type) with few exceptions of magnetite (I-type) series occurrences (Figure 17). The MS values range from 0.01 to 44.4 $\times$ 10^{-3} SI for both series. Only four of these values

are above 3×10^{-3} SI indicating I-type, magnetite series. Most values are below 3×10^{-3} SI pointing to S-type, ilmenite series in the sample population. The Central Gold Belt is characterized by numerous occurrences of sediment-hosted gold deposits which are both intruded by S-type and I-type granitoids. But in the Gua Musang area, they are mostly S-type granites present as shown in this study, and further south close to the Bentong area, some I-type granites were found. MS data are documented in Table S8.

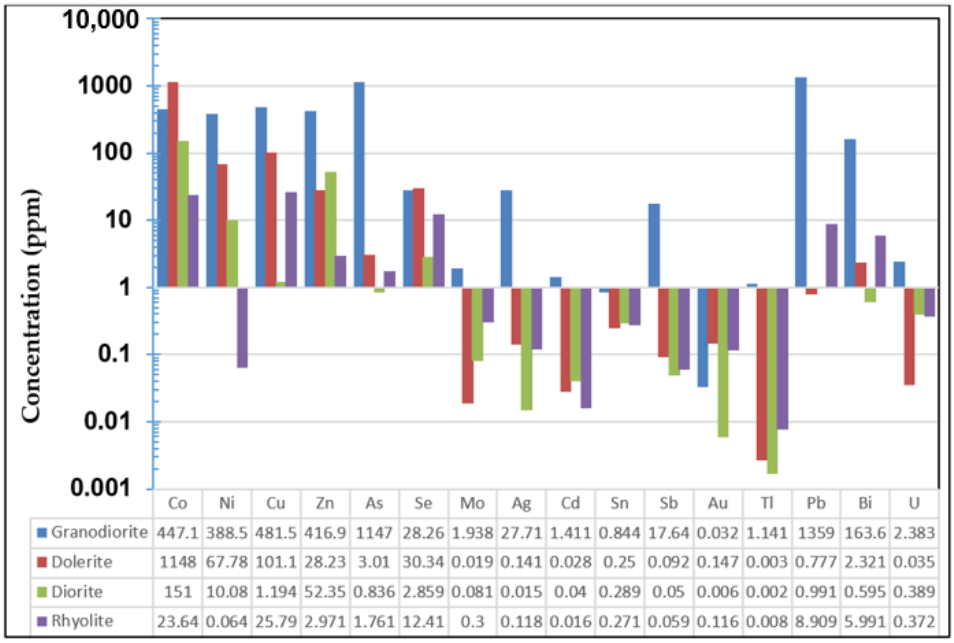

	Co	Ni	Cu	Zn	As	Se	Mo	Ag	Cd	Sn	Sb	Au	Tl	Pb	Bi	U
Granodiorite	447.1	388.5	481.5	416.9	1147	28.26	1.938	27.71	1.411	0.844	17.64	0.032	1.141	1359	163.6	2.383
Dolerite	1148	67.78	101.1	28.23	3.01	30.34	0.019	0.141	0.028	0.25	0.092	0.147	0.003	0.777	2.321	0.035
Diorite	151	10.08	1.194	52.35	0.836	2.859	0.081	0.015	0.04	0.289	0.05	0.006	0.002	0.991	0.595	0.389
Rhyolite	23.64	0.064	25.79	2.971	1.761	12.41	0.3	0.118	0.016	0.271	0.059	0.116	0.008	8.909	5.991	0.372

Figure 16. Chart showing variations in trace element contents across igneous-rock hosted pyrites. Diorite-hosted pyrites have the lowest gold content. At the bottom, the diagram which is combined with the legend shows the mean values of each element found in the collected samples.

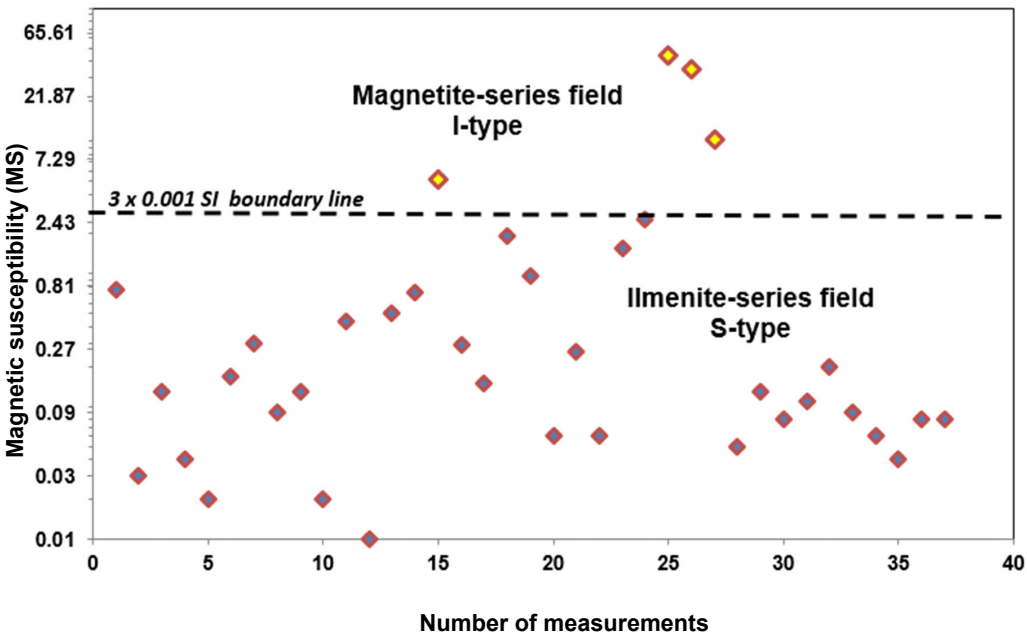

Figure 17. Spider plot of magnetic susceptibility (MS) measurements for the granitic samples collected in the study area. The dotted line sits at the value of 3×10^{-3} SI discriminating the I-type and S-type granites. All I-type samples plot above the line 3×0.001 SI and the S-type samples plot below the line 3×0.001 SI.

6. Discussion

6.1. Zircon Age Dating

The mineral zircon has extensively been used to date sedimentary, metamorphic and magmatic rocks. In this study, the CL images combined with the ratio Th/U > 0.1 for most samples suggest that the zircon crystals derived from a magmatic protolith. Only two Th/U ratio values plot immediately below the Th/U = 0.1 line, indicating that these values may point to a metamorphic origin of the zircons. Previous works have indicated that Th/U > 0.1 links to a magmatic origin of the zircons [58,59]. However, samples with Th/U < 0.1 and displaying no internal zoning or being weakly zoned point to a metamorphic protolith [60–62]. Most samples collected in the Bentong-Raub Suture Zone plot along the line Th/U = 1, which indicate an increase in the Th content relative to U content in the zircon samples as shown in Figure 18.

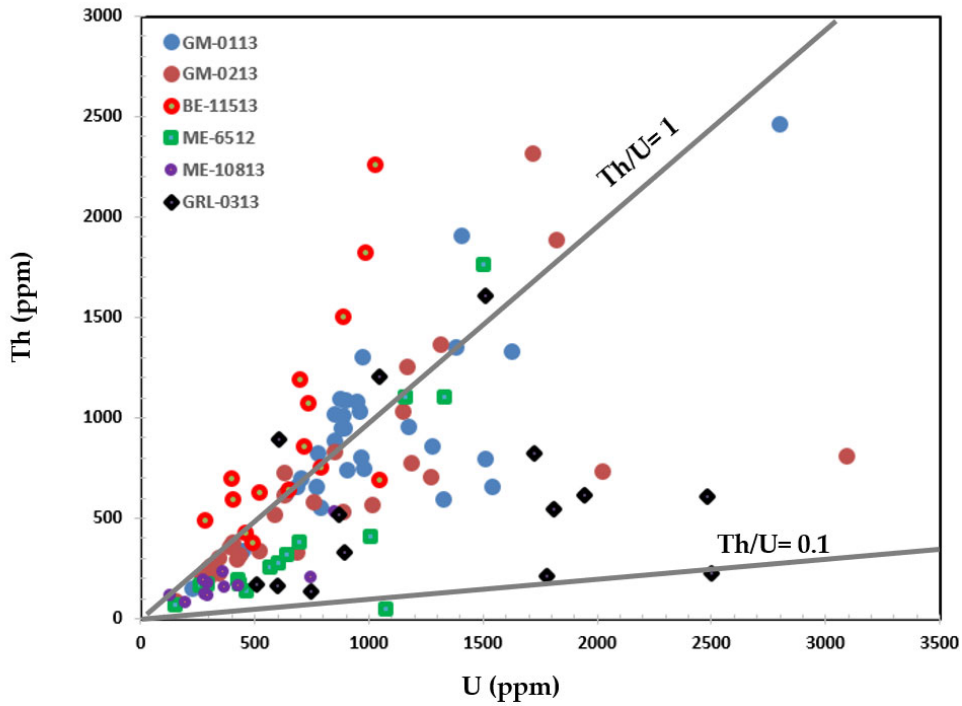

Figure 18. Binary plot of Th versus U for the zircon samples. As shown in the legend, samples GM-0113 and GM-0213 came from the Gua Musang area. Sample BE-11513 was collected from the Bentong area along the suture. Sample ME-6512 and ME-10813 were collected from the Semantan Formation. Sample GRL-0313 was collected from Langkawi Islands, far from the Bentong-Raub Suture Zone.

U-Pb zircon dating of Malaysian granitoids was undertaken by previous researchers to determine the ages of magmatism for the S-and I-type granitoids and contribute to the ongoing reconstruction of the Malaysian tectonic history [38,63–65]. In this study, the ages of zircon range between 204.1 ± 4.7 Ma and 223.7 ± 3.2 Ma. It can be noted that the age of 223.7 ± 3.2 Ma is found within the age range (226–220 Ma) of the Central Belt granitoids [66]. Comparatively, zircon ages are younger (204.1 to 205.6 Ma) close to the suture zone and, older far from the suture in the Bentong area (223.7 Ma).

This study also shows that U-Pb zircon dating of tuffaceous sediments from the Semantan Formation, which crops out south of the orogenic deposits, indicates an age of 233.1 ± 1.6 Ma (Middle Triassic-Ladinian) which is higher than the age of granitic crystallization by 10 Ma. The ages 204.1, 205.6, and 208.1 Ma come from granitic rocks found in the Gua Musang area in the vicinity of gold deposits such as the Tersang and Selinsing gold deposits.

6.2. Pb Isotopes and Age of Gold Mineralization

To better understand the relationship between Pb isotope model age and the age of gold mineralization, Figures 12 and 13 should be looked at side by side. Figure 12 shows the Pb isotope model age of K-feldspar from I-type granitoids found in the Gua Musang area. The GM ellipse plots around 200 Ma. Figure 13 shows that the Pb isotope model age of pyrite core which has both gold and Pb concentrations has an age of 200 Ma.

The Pb isotope compositions of pyrite cores at the Selinsing and Tersang gold deposits approximate the Pb-Pb model age around 200 Ma. This suggests that the age of the gold mineralization is most likely 200 Ma (Figure 13), coinciding with the Pb-Pb model age on K-feldspar (i.e., 200 Ma) from the analyzed ilmenite-series granitoids from the Gua Musang area (Figure 11). In this study, the age of gold mineralization can be constrained from the Pb isotope model age of gold-bearing pyrite core, which is 200 Ma. The age of 200 Ma from Pb isotope composition of K-feldspar from I-type granitoid samples could point to a magmatic contribution to Au mineralization. This goes with the evidence that these I-type granitoid rock samples contain gold-bearing pyrite (up to 793 ppb Au), as shown in Table S6.

Early researchers speculated that the gold mineralization in central mainland Malaysia may be associated with igneous rocks [1,67,68]. Later, further research constrained the age of gold mineralization using K-Ar age dating of sericite and returned an age range of 197–199 Ma (Early Jurassic) from tonalite cropping out at the Penjom gold deposit [3]. Considering the present study, the age of gold mineralization is estimated to be 200 Ma. Compared to previous studies, K/Ar dating of sericite separates yielded stable ages of 194–191 Ma [69]). This age is close to the 200 Ma Pb model age.

The Pb isotope composition of pyrite from the Semantan tuffaceous black shales is slightly less radiogenic than that of K-feldspar from S-type granites that crop out in the Central Belt implying some discrepancies in the Pb-Pb model age. Although the age of the granites and ores may be similar, there are small differences in the Pb isotopic composition of the ores and that of the granite and sedimentary pyrite. The sedimentary pyrites and granite K-feldspars plot on a high μ (high U/Pb) growth curve typical of S-type granites and sediments but the ores tend to plot on the bulk crustal growth curve, suggesting a greater proportion of mantle Pb relative to upper crustal Pb. This mantle Pb could be partly sourced from I-type granitic rocks, mafic rocks, or arc-related volcanic rocks.

6.3. Pyrite Trace Elements

Correlation coefficients are used to check how strong a relationship is between two variables. As shown in Table S8, gold correlates well with Cu, Ag, Cd, Te, and Pb in the diorite. In the granodiorite, Au correlates well with Cu, Zn, Cd, Te, and Pb. In the rhyolite, Au correlates well with Cu, Zn, As, Sn, Sb, Te, and Pb. In the dolerite, Au shows good correlation with Ni, Cu, and Te. Some of the gold deposits in Malaysia are intrusion-related such as the Tersang gold deposit which has a rhyolite corridor crosscutting the sedimentary sequences [3]. This study reveals that elements such as Te, Cu, and Pb which consistently correlate with gold in all the pyrite samples may serve as geochemical indicators to Au mineralization for auriferous environments associated with magmatic intrusions. However, Te, Cu, and Pb are not the only pathfinders for gold. In other regions, arsenic may be a good pathfinder for gold. In this study, it is also shown that gold correlates well with arsenic in the rhyolite samples. In the Tersang area where there is a rhyolite corridor (Figure 4), arsenic could be a good pathfinder for gold.

6.4. Timing of Gold Mineralization Relative to Volcanism

Studies such as [3] documented that in the Central Belt, gold mineralization may be associated with volcanism in the study area. In this study, field observation has shown that the Semantan black shales are associated with tuffs which strongly indicate that volcanism in the area occurred during deposition of the shales. The age of these tuffs is 233.1 ± 1.6 Ma, indicating a Middle Triassic age (Ladinian) for the volcanism. The present research outcomes show an unclear temporal relationship between gold mineralization and

volcanic activity due to the 33 Ma age gap between 200 Ma (Pb-Pb model age in the core of gold-bearing pyrite) and 233.1 Ma (zircon age of the volcaniclastic rocks). The timing of gold mineralization in the study area likely post-dates volcanic activities.

6.5. Exploration Implications

Considering the present study, two parameters can be taken into consideration: the age of gold mineralization and the chemical composition of pyrite in granitoids that intruded the sedimentary sequences. The age of gold mineralization which is estimated to be 200 Ma using the Pb-Pb model age of pyrite, can help target undiscovered mineralized zones in the Tersang district, Malaysia. Based on coefficients of correlation, the elemental relationship between Au and other elements is as follows:

1. Au (Cu, Ag, Cd, Te, Pb)—for diorite-hosted pyrite
2. Au (Cu, Zn, Cd, Te)—for granodiorite-hosted pyrite
3. Au (Cu, Ni, Ag, Te, Pb)—for dolerite-hosted pyrite
4. Au (Cu, Zn, As, Sn, Sb, Te, Pb)—for rhyolite-hosted pyrite

In this study, the above elemental associations show that Au has a consistent and strong correlation, particularly with elements such as Cu, Te, Pb, Ag, and Cd. These elements can be used as pathfinders in the search for orogenic gold deposits. It was found that Au is associated with Cu in the Shicheng Au-Cu deposit across the Muping-Rushan metallogenic belt in southeast Jiaodong, China [70]. The Shicheng Au-Cu deposit is hosted in the Late Early Cretaceous Sanfoshan pluton and is characterized by Au-Cu-bearing quartz-carbonate-sulfide veins.

The use of Pb isotope composition in pyrite can also constrain the age of gold mineralization in brownfield and greenfield exploration. This approach should be combined with pyrite elemental mapping and trace element chemistry using LA ICP-MS technology. Pyrite samples that have an appreciable amount of gold and lead with distinct Au and Pb zoning patterns are the best candidates. The composition of trace elements in pyrite hosted in granitoids and the relationship between gold and trace elements will help determine accompanying pathfinders. This exploration strategy can be applied both in Malaysia and around the world.

7. Conclusions

The selected S-type granitoid rocks in the Central Belt yield crystallization ages ranging from 204.1 ± 4.7 Ma to 223 ± 3.2 Ma with low magnetic susceptibility measurements. The gold content in pyrite shows oscillatory patterns together with lead for most samples collected from the Tersang and Selinsing gold deposits. The Pb isotope model age of 200 Ma obtained in gold-enriched pyrite core implies that the age of gold mineralization is 200 Ma as evidenced by close association of Au and Pb pyrite images. The connection between gold mineralization and volcanism is unlikely due to a gap of 33 Ma of the age difference between the isotopic model age of gold mineralization (200 Ma) in the pyrite core and the zircon age of the volcaniclastic rocks (233 Ma). Gold content was found to be up to 800 ppb in the analyzed magmatic rocks implying a genetic relationship between the gold occurrence and granitoid emplacement. In this research, Au shows a consistent and strong correlation with elements such as Cu, Te, Pb, Ag, and Cd. These elements can be used as pathfinders in the search for orogenic gold deposits.

Supplementary Materials: The following supporting information can be downloaded at: https://www.mdpi.com/article/10.3390/min13020221/s1, Table S1: Geochronology data; Table S2: Pb isotope composition of K-Feldspar from granitoids; Table S3: Pb isotope composition of pyrite from other formations far from the ore deposits; Table S4: Pb isotope composition of pyrite from gold deposits; Table S5: Pb208 and gold content in count per second; Table S6: Trace element composition of pyrite; Table S7: Coefficients of correlation; Table S8: Magnetic susceptibility data.

Author Contributions: For this research article, author individual contributions are the following: Conceptualization, C.M., Z.E. and K.Z.; methodology, C.M. and Z.E.; software, C.M.; validation, C.M.; formal analysis, C.M.; investigation, C.M.; resources, Z.E.; data curation, C.M.; writing—original draft preparation, C.M.; writing—review and editing, C.M. and Z.E.; visualization, C.M. and Z.E.; supervision, C.M.; project administration, C.M.; funding acquisition, C.M. All authors have read and agreed to the published version of the manuscript.

Funding: This research was funded by the University of Tasmania–APA Scholarship and the Southeast Asia Ore Deposit Research Projects.

Data Availability Statement: The data is contained within the article or Supplementary Material.

Acknowledgments: The authors are thankful for the support from the Project "Ore Deposits of SE Asia Project" and the University of Tasmania-APA (Australian Postgraduate Award) Ph.D. Scholarship. Special thanks are due to Sebastien Meffre for his assistance and suggestions during the lead isotope analysis. Much appreciation to Leonid Danyushevsky and his technical team for their help on LA ICP-MS analysis of pyrite at the CODES laboratory facility, University of Tasmania, Australia. This paper is part of the first author MSc and Ph.D. research project undertaken at the Centre for Ore Deposit and Earth Sciences (CODES), University of Tasmania, Australia.

Conflicts of Interest: The authors declare no conflict of interest.

References

1. Richardson, J.A. The Geology and mineral resources of the neighborhood of Raub, Pahang with an account of the Geology of the Raub Australian Gold Mine. *Geol. Surv. Malays. Kuala Lumpur* **1939**, *3*, 166.
2. Yeap, E.B. Tin and gold mineralization in Peninsular Malaysia and their relationships to the tectonic development. *J. Southeast Asian Earth Sci.* **1993**, *8*, 329–348. [CrossRef]
3. Makoundi, C. Geology, Geochemistry and Metallogenesis of Selected Sediment-hosted gold deposits in the Central Gold Belt, Peninsular Malaysia. Master's Thesis, University of Tasmania, Hobart, Australia, 2012.
4. Zaw, K.; Meffre, S.; Lai, C.-K.; Burrett, C.; Santosh, M.; Graham, I.; Manaka, T.; Salam, A.; Kamvong, T.; Cromie, P. Tectonics and metallogeny of mainland Southeast Asia—A review and contribution. *Gondwana Res.* **2014**, *26*, 5–30.
5. Makoundi, C.; Zaw, K.; Large, R.R.; Meffre, S.; Lai, C.K.; Hoe, T.G. Geology, geochemistry, and metallogenesis of the Selinsing gold deposit, Central Malaysia. *Gondwana Res.* **2014**, *26*, 241–261. [CrossRef]
6. Endut, Z.; Tham Fatt, N.G.; Abdul Aziz, J.H.; Meffre, S.; Makoundi, C. Characterization of Galena and Vein Paragenesis in the Penjom Gold Mine, Malaysia: Trace Elements, Lead Isotope Study and Relationship to Gold Mineralization Episodes. *Acta Geol. Sin.* **2015**, *89*, 1801–1840.
7. Makoundi, C. Geochemistry of Black Shales, Sandstones; Chert in Malaysia: Insights into Gold Source Rocks. Ph.D. Thesis, University of Tasmania, Hobart, Australia, 2016.
8. Makoundi, C.; Zaw, K.; Large, R. Laser Ablation ICPMS Analysis of Pyrite and U-Pb Zircon Dating of Host Rocks from the Tersang Gold Deposit, Malaysia. *AIMS Geosci.* **2017**, *3*, 396–437. [CrossRef]
9. Zatman, R.E.; Stacey, J.S. Lead isotope and mineralization ages in belt supergroup rocks, Northwestern Montana and Northern Idaho. *Econ. Geol.* **1971**, *66*, 849–860. [CrossRef]
10. Zatman, R.E.; Doe, B.R. Plumbotectonics—the model. *Tectonophysics* **1981**, *75*, 135–162. [CrossRef]
11. Gulson, B.L. Lead isotopes in mineral exploration. *Dev. Econ. Geol.* **1986**, *23*, 1–245.
12. Rollinson, H.R. *Using Geochemical Data: Evaluation, Presentation, Interpretation*; Routledge: Abingdon-on-Thames, UK, 1996.
13. Cannon, R.S.; Pierce, A.P.; Antweiler, J.C.; Buck, K.L. The data of lead isotope geology related to problems of ore genesis. *Econ. Geol.* **1961**, *56*, 1–38. [CrossRef]
14. Meffre, S.; Large, R.R.; Scott, R.; Woodhead, J.; Chang, Z.; Gilbert, S.E.; Danyushevsky, L.V.; Maslennikov, V.; Hergt, J.M. Age and pyrite Pb-isotopic composition of the giant Sukhoi Log sediment-hosted gold deposit, Russia. *Geochim. et Cosmochim. Acta* **2008**, *72*, 2377–2391. [CrossRef]
15. Large, R.R.; Maslennikov, V.V.; Robert, F.; Danyushevsky, L.V.; Chang, Z. Multistage Sedimentary and Metamorphic Origin of Pyrite and Gold in the Giant Sukhoi Log Deposit, Lena Gold Province, Russia. *Econ. Geol.* **2007**, *102*, 1233–1267. [CrossRef]
16. Large, R.R.; Danyushevsky, L.; Hollit, C.; Maslennikov, V.; Meffre, S.; Gilbert, S.; Bull, S.; Scott, R.; Emsbo, P.; Thomas, H.; et al. Gold and Trace Element Zonation in Pyrite Using a Laser Imaging Technique: Implications for the Timing of Gold in Orogenic and Carlin-Style Sediment-Hosted Deposits. *Econ. Geol.* **2009**, *104*, 635–668. [CrossRef]
17. Ding, L.; Zhu, L.; Yuan, H.; Lu, R.; Xiong, X.; Yang, T. Geology, Pb Isotope Geochemistry and Ore Genesis of the Liziyuan Gold Deposit, West Qinling Orogen, Central China. *Acta Geol. Sin. Engl. Ed.* **2018**, *92*, 1082–1099. [CrossRef]
18. Li, S.; Chen, C.; Gao, L.; Xia, F.; Zhang, X.; Wang, K.; Arkin, K. Ore Genesis of the Kuergasheng Pb–Zn Deposit, Xinjiang Province, Northwest China: Constraints from Geology, Fluid Inclusions, and H–O–C–S Isotopes. *Minerals* **2020**, *10*, 592. [CrossRef]

19. Mann, S.; Sparks, N.H.C.; Frankel, R.B.; Bazylinski, D.A.; Jannasch, H.W. Biomineralization of ferromagnetic greigite (Fe3S4) and iron pyrite (FeS2) in a magnetotactic bacterium. *Nature* **1990**, *343*, 258–261. [CrossRef]
20. Reich, M.; Deditius, A.; Chryssoulis, S.; Li, J.W.; Ma, C.Q.; Parada, M.A.; Barra, F.; Mittermayr, F. Pyrite as a record of hydrothermal fluid evolution in a porphyry copper system: A SIMS/EMPA trace element study. *Geochim. Cosmochim. Acta* **2013**, *104*, 42–62. [CrossRef]
21. Castellón, C.I.; Toro, N.; Gálvez, E.; Robles, P.; Leiva, W.H.; Jeldres, R.I. Froth Flotation of Chalcopyrite/Pyrite Ore: A Critical Review. *Materials* **2022**, *15*, 6536. [CrossRef]
22. Huston, D.L.; Sie, S.H.; Suter, G.F.; Cooke, D.R.; Both, R.A. Trace-elements in sulfide minerals from eastern Australian volcanic-hosted massive sulfide deposits. 1. Proton microprobe analyses of pyrite, chalcopyrite; sphalerite; 2. Selenium levels in pyrite—comparison with delta-s-34 values and implications for the source of sulfur in volcanogenic hydrothermal systems. *Econ. Geol.* **1995**, *90*, 1167–1196.
23. Deditius, A.P.; Utsunomiya, S.; Reich, M.; Kesler, S.E.; Ewing, R.C.; Hough, R.; Walshe, J. Trace metal nanoparticles in pyrite. In Proceedings of the Goldschmidt Conference 2010, Knocville, TN, USA, 13–18 June 2010.
24. Wakita, K.; Metcalfe, I. Ocean Plate Stratigraphy in East and Southeast Asia. *J. Asian Earth Sci.* **2005**, *24*, 679–702. [CrossRef]
25. Keppie, D.F. How the closure of paleo-Tethys and Tethys oceans controlled the early breakup of Pangaea. *Geology* **2015**, *43*, 335–338. [CrossRef]
26. Dong, J.; Zou, H.; Liu, H.; Li, Y.; Jiang, X. The Mesozoic Closure of the Paleo-Tethys Ocean: Constraints from Zircon U–Pb Ages, Hf and Nd Isotopes of the Granitic Plutons in the Hoh-Xil-Songpan-Ganzi. *J. Coast. Res.* **2019**, *94*, 101–106. [CrossRef]
27. Metcalfe, I. The Bentong-Raub Suture Zone. *J. Asian Earth Sci.* **2000**, *18*, 691–712. [CrossRef]
28. Schwartz, M.; Rajah, S.; Askury, A.; Putthapiban, P.; Djaswadi, S. The Southeast Asian tin belt. *Earth Sci. Rev.* **1995**, *38*, 95–293. [CrossRef]
29. Kobayashi, T.; Tamura, M. Myophoria in Malaya with a note on the Triassic Trigoniacea. In *Geology and Paleontology of Southeast Asia*; Kobayashi, T., Toriyama, R., Eds.; the University of Tokyo Press: Tokyo, Japan, 1968; pp. 88–137.
30. Makoundi, C. Facies analysis of the Triassic Jelai Formation in the Central Basin of Peninsular Malaysia: Implications on paleogeography and tectonics. Master's Thesis, University of Malaya, Kuala Lumpur, Malaysia, 2004.
31. Proctor, W.D. Geology and Mineral Resources Benta area, Pahang. Geological Survey of Malaysia. *Map Bull.* **1972**, *4*, 25.
32. Gobbett, D.J.; Hutchison, C.S. *Geology of the Malay Peninsular: West Malaysia and Singapore*; Wiley: Hoboken, NJ, USA, 1973; p. 438.
33. Tan, B.K. The tectonic framework and evaluation of the Central Belt and its margin, Peninsular Malaysia. *Geol. Soc. Malays. Bull.* **1984**, *17*, 307–322. [CrossRef]
34. Leman, M.S. The significance of Upper Permian Brachiopods from Merapoh area, northwest Pahang. *Geol. Soc. Malays. Bull.* **1994**, *35*, 113–121. [CrossRef]
35. Metcalfe, I. Permian tectonic framework and palaeogeography of SE Asia. *J. Asian Earth Sci.* **2002**, *20*, 551–566. [CrossRef]
36. Mustaffa, K.; Hadi, A.; Rahman, A. A fivefold stratigraphic and tectonic subdivision of Peninsular Malaysia. In *Dynamic stratigraphy and tectonics of Peninsular Malaysia—Problems and Issues*; Geological Society of Malaysia: Kuala Lumpur, Malaysia, 1999; pp. 38–63.
37. Oliver, G.; Zaw, K.; Hoston, M. Dating rocks in Singapore: Plate tectonics between 280 and 200 million years ago. *Singap. Mag. Res.* **2011**, *10*, 23–25.
38. Bignell, J.D.; Snelling, N.J. K-Ar ages on some basic igneous rocks from Peninsular Malaysia and Thailand. *Bull. Geol. Soc. Malays.* **1977**, *8*, 89–93. [CrossRef]
39. Liew, T.C.; McCulloch, M.T. Genesis of granitoid batholiths of Peninsular Malaysia and implications for models of crustal evolution: Evidence from Nd-Sr isotopic and U-Pb zircon study. *Geochim. Cosmochim. Acta* **1985**, *49*, 587–600. [CrossRef]
40. Ghani, A.A. Geochemical characteristics of S- and I-Type Granites: Example from Peninsular Malaysia granites. *Bull. Geol. Soc. Malays.* **2005**, *51*, 123–134. [CrossRef]
41. Makoundi, C.; Zaw, K.; Endut, Z. Fluid Inclusion Study of the Penjom, Tersang, and Selinsing Orogenic Gold Deposits, Peninsular Malaysia. *Minerals* **2020**, *10*, 111. [CrossRef]
42. Wiedenbeck, M.A.; Alle, P.; Corfu, F.; Griffin, W.L.; Meier, M.; Oberli, F.V.; von Quadt, A.; Roddick, J.C.; Spiegel, W. Three natural zircon standards for U-Th-Pb, Lu-Hf, trace element and REE analyses. *Geostand. Newsl.* **1995**, *19*, 1–23. [CrossRef]
43. Black, L.P.; Kamo, S.L.; Allen, C.M.; Aleinikoff, J.N.; Davis, D.W.; Korsch, R.J.; Foudoulis, C. TEMORA 1: A new zircon standard for Phanerozoic U–Pb geochronology. *Chem. Geol.* **2003**, *200*, 155–170. [CrossRef]
44. Jackson, S.E.; Pearson, N.J.; Griffin, W.L.; Belousova, E.A. The application of laser ablation-inductively coupled plasma-mass spectrometry to in situ U–Pb zircon geochronology. *Chem. Geol.* **2004**, *211*, 47–69. [CrossRef]
45. Black, L.P.; Gulson, B.L. The age of the Mud tank Carbonatite, Strangways Range, Northern Territory. *BMR J. Aust. Geol. Geophys.* **1978**, *3*, 227–232.
46. Baker, J.; Peate, D.; Waight, T.; Meyzen, C. Pb isotopic analysis of standards and samples using a Pb207/Pb204 double spike and thallium to correct for mass bias with a double-focusing MC-ICP-MS. *Chem. Geol.* **2004**, *211*, 275–303. [CrossRef]
47. Black, L.P.; Kamo, S.L.; Allen, C.M.; Davis, D.W.; Aleninikoff, J.N.; Valley, J.W.; Mundil, R.; Campbell, I.H.; Korsch, R.J.; Williams, I.S.; et al. Improved 206Pb/238U microprobe geochronology by the monitoring of a trace-element related matrix effect; SHRIMP, ID-TIMS, ELA-ICP-MS; oxygen isotope documentation for a series of zircon standards. *Chem. Geol.* **2004**, *205*, 115–140. [CrossRef]

48. Paton, C.; Woodhead, J.D.; Hellstrom, J.C. Improved laser ablation U-Pb zircon geochronology through robust down-hole fractionation correction. *Geochem. Geophys. Geosyst.* **2010**, *11*, 1525–2027. [CrossRef]
49. Kosler, J. Laser-ablation ICPMS study of metamorphic minerals and processes. In *Laser-Ablation-ICPMS in the Earth Sciences; Principles and Applications: Mineralogical Association of Canada Short Course Handbook*; Sylvester, P.J., Ed.; Mineralogical Association of Canada: Vancouver, BC, Canada, 2001; pp. 185–202.
50. Danyushevsky, L.V.; Robinson, P.; Gilbert, S.; Norman, M.; Large, R.R.; McGoldrick, P.; Shelley, J.M.G. Routine quantitative multi-element analysis of sulfide minerals by laser ablation ICP-MS: Standard development and consideration of matrix effects. *Geochem. Explor. Environ. Anal.* **2011**, *11*, 51–60. [CrossRef]
51. Belousov, I. New calibration standard for LA-ICPMS analysis of sulphides. AGU, 2014 Fall Meeting. Available online: https://agu.confex.com/agu/fm14/webprogram/Paper19453.html (accessed on 30 June 2021).
52. Belousov, I.A.; Danyushevsky, L.V.; Olin, P.H.; Gilbert, S.E.; Thompson., J. STDGL3: A new calibration standard for sulphide analysis by LAICP-MS. In Proceedings of the 25th Goldschmidt Conference, Prague, Czech Republic, 16–21 August 2015.
53. Jochum, K.; Enzweiler, J. *Reference Materials in Geochemical and Environmental Research. Analytical Geochemistry/Inorganic Instrumental Analysis*, 2nd ed.; Elsevier Ltd.: Amsterdam, The Netherlands, 2014; Volume 15, pp. 43–70.
54. Gilbert, S.E.; Danyushevsky, L.V.; Rodemann, T.; Shimizu, N.; Gurenko, A.; Meffre, S.; Thomas, H.; Large, R.R.; Death, D. Optimisation of laser parameters for the analysis of sulphur isotopes in sulphide minerals by laser ablation ICP-MS. *J. Anal. At. Spectrom.* **2014**, *29*, 1042–1051. [CrossRef]
55. Maulana, A.; Watanabe, K.; Imai, A.; Yonezu, K. Origin of Magnetite- and Ilmenite-series Granitic Rocks in Sulawesi, Indonesia: Magma Genesis and Regional Metallogenic Constraint. *Procedia Earth Planet. Sci.* **2013**, *6*, 50–57. [CrossRef]
56. Villaseca, C.; Ruiz-Martinez, V.C.; Perez-Soba, C. Magnetic susceptibility of Variscan granite-types of the Spanish Central System and the redox state of magma. *Geol. Acta Int. Earth Sci. J.* **2017**, *15*, 379–394. [CrossRef]
57. Stacey, J.S.; Kramer, J.D. Approximation of terrestrial lead isotope evolution by a two-stage model. *Earth Planet. Sci. Lett.* **1975**, *26*, 207–221. [CrossRef]
58. Hoskin, P.W.O.; Schaltegger, U. The Composition of Zircon and Igneous and Metamorphic Petrogenesis. *Rev. Miner. Geochem.* **2003**, *53*, 27–62. [CrossRef]
59. Xie, W.; Lu, Y.; Chen, L.-M.; Song, X.-Y.; Deng, Y.-F.; Zhao, Y. Zircon Th/U ratios suggest a post-collision extensional setting for the Permian Ni-Cu sulfide deposits in the Eastern Tianshan, NW China. *Ore Geol. Rev.* **2022**, *144*, 104837. [CrossRef]
60. Wu, Y.; Zheng, Y. Genesis of zircon and its constraints on interpretation of U-Pb age. *Chin. Sci. Bull.* **2004**, *49*, 1554–1569. [CrossRef]
61. Lopez-Sanchez, M.A.; Aleinikoff, J.N.; Marcos, A.; Martínez, F.J.; Llana-Fúnez, S. An example of low-Th/U zircon overgrowths of magmatic origin in a late orogenic Variscan intrusion: The San Ciprián massif (NW Spain). *J. Geol. Soc.* **2015**, *173*, 282–291. [CrossRef]
62. Castineiras, P.; Barneiro, J.G.; Fernandez, F.J.; Aguilar, C.; Perez, J.M.B. Reso;ving uncertainties in the application of zircon Th/U and CL gauges to interpret U-Pb ages: A case study of eclogites in polymetamorphic terranes of NW Iberia. *Solid Earth Discuss.* **2020**, *14*, 1–21. [CrossRef]
63. Darbyshire, D.P.F. South-East Asia Granite Project: Geochronology of Malaysian Granites. *Nat. Environ. Res. Counc. Isot. Geol.* **1988**, *88*, 60.
64. Ghani, A.A.; Searle, M.P.; Robb, L.J.; Chung, S.-L. Transitional I-S type characteristic in the Main Range Granite, Peninsular Malaysia. *J. Asian Earth Sci.* **2013**, *76*, 225–240. [CrossRef]
65. Metcalfe, I. Tectonic evolution of the Malay Peninsula. *J. Asian Earth Sci.* **2013**, *76*, 195–213. [CrossRef]
66. Ng, S.W.-P.; Whitehouse, M.; Searle, M.P.; Robb, L.J.; Ghani, A.A.; Chung, S.-L.; Oliver, G.J.; Sone, M.; Gardiner, N.; Roselee, M.H. Petrogenesis of Malaysian granitoids in the Southeast Asian tin belt: Part 2. U-Pb zircon geochronology and tectonic model. *GSA Bull.* **2015**, *127*, 1238–1258. [CrossRef]
67. Scrivenor, J.B. *The Geology of Malayan Ore Deposits*; Macmillan: London, UK, 1928; 216p.
68. Ingham, F.T. The geology of the neighborhood of Tapah and Telok Anson, Perak, F.M.S with accounts of mineral deposits. *Geol. Surv. Dep. Fed. Malaya Mem.* **1938**, *2*, 72.
69. Bogie, I. *Petrology Report on 15 Samples from the Penjom Gold Mine, Malaysia; Internal Report for Specific Resources*, Sdn. Bhd: Malaysia, 2002.
70. Elshourbagi, H.M.; Fan, H.-R. An oxidized intrusion-related origin in the controversial Jiaodong gold province (China) for the Shicheng Au-Cu deposit. *All Earth* **2021**, *33*, 5–29. [CrossRef]